Received: 2 July 2020 | Revised: 12 December 2020 | Accepted: 14 December 2020

DOI: 10.1002/esp.5056

RESEARCH ARTICLE

ESPL WILEY

Modelling future lahars controlled by different volcanic eruption scenarios at Cotopaxi (Ecuador) calibrated with the massively destructive 1877 lahar

Theresa Frimberger[1] | S. Daniel Andrade[2] | Samuel Weber[1] | Michael Krautblatter[1]

[1]Landslide Research Group, Technical University of Munich, Munich, Germany

[2]Instituto Geofísico, Escuela Politécnica Nacional, Quito, Ecuador

Correspondence
Theresa Frimberger, Landslide Research Group, Technical University of Munich, Munich, Germany.
Email: theresa.frimberger@tum.de

Funding information
Bundesministerium für Bildung und Forschung, Grant/Award Number: 03G0876D

Abstract

Lahars are among the most hazardous mass flow processes on earth and have caused up to 23 000 casualties in single events in the recent past. The Cotopaxi volcano, 60 km southeast of Quito, has a well-documented history of massively destructive lahars and is a hotspot for future lahars due to (i) its ~10 km^2 glacier cap, (ii) its 117–147-year return period of (Sub)-Plinian eruptions, and (iii) the densely populated potential inundation zones (300 000 inhabitants). Previous mechanical lahar models often do not (i) capture the steep initial lahar trajectory, (ii) reproduce multiple flow paths including bifurcation and confluence, and (iii) generate appropriate key parameters like flow speed and pressure at the base as a measure of erosion capacity. Here, we back-calculate the well-documented 1877 lahar using the RAMMS debris flow model with an implemented entrainment algorithm, covering the entire lahar path from the volcano edifice to an extent of ~70 km from the source. To evaluate the sensitivity and to constrain the model input range, we systematically explore input parameter values, especially the Voellmy–Salm friction coefficients μ and ξ. Objective selection of the most likely parameter combinations enables a realistic and robust lahar hazard representation. Detailed historic records for flow height, flow velocity, peak discharge, travel time and inundation limits match best with a very low Coulomb-type friction μ (0.0025–0.005) and a high turbulent friction ξ (1000–1400 m/s^2). Finally, we apply the calibrated model to future eruption scenarios (Volcanic Explosivity Index = 2–3, 3–4, >4) at Cotopaxi and accordingly scaled lahars. For the first time, we anticipate a potential volume growth of 50–400% due to lahar erosivity on steep volcano flanks. Here we develop a generic Voellmy–Salm approach across different scales of high-magnitude lahars and show how it can be used to anticipate future syneruptive lahars.

KEYWORDS
debris flow erosion, lahar, model calibration, numerical model, predictive modelling

1 | INTRODUCTION

The Indonesian term 'lahar' refers to a rapidly flowing mixture of sediment and water that originates from a volcano (Smith & Fritz, 1989), either directly related to eruptive activity (i.e. primary/syneruptive lahar) or during post-eruptive periods (i.e. secondary lahar). These mass flows rank among the most disastrous volcanic natural hazards (Auker et al., 2013). The destructive potential of lahars arises from their sudden onset and outstanding flow characteristics (featured by high sediment-carrying capacity), speeds exceeding tens of kilometres

per hour, discharges up to about 50 000 m^3/s, and runout distances of tens to even hundreds of kilometres (Mothes et al., 2004; Thouret et al., 2020). About 56 000 lahar-related fatalities have been documented since 1500 AD (Brown et al., 2017), including about 23 000 fatalities at Nevado del Ruíz in Colombia in 1985 (Pierson et al., 1990). As population density and infrastructure development close to active volcanoes is rapidly growing, an increasing number of people are potentially exposed to volcanic hazards (Auker et al., 2013; Small & Naumann, 2001). In the last few decades, efforts have been made to reduce the risk to human life by implementing effective monitoring and early-warning systems, and by assessing probable lahar inundation areas through modelling and reconstruction of the eruptive history. The active, glacier-capped Cotopaxi volcano is among the most dangerous volcanoes worldwide, because it can produce very large eruption-triggered lahars, which may inundate densely inhabited valleys close to the volcano. In this study, we aim to contribute to the hazard assessment of syneruptive lahars by testing the applicability of a Voellmy-based debris flow model including entrainment and analysing its capability to reproduce key characteristics of lahars.

1.1 | Characteristics of lahars

The flow behaviour of lahars is strongly influenced by sediment concentration, type of sediment and particle size distribution (Pierson et al., 1987; Vallance & Iverson, 2015), and can range from hyperconcentrated flows, which transport between 5–10 and 20–60 vol% of solids and show bulk densities of 1300–1800 kg/m^3 (Beverage & Culbertson, 1964; Pierson, 2005), to debris flows with solids concentration exceeding 20–60 vol% and bulk densities varying between 1800 and 2300 kg/m^3 (Costa, 1984; Iverson, 1997; McArdell et al., 2007). Several field studies have revealed reversible lahar phase transitions during downstream propagation (Pierson & Scott, 1985; Scott, 1988) as lahars incorporate (bulking) or deposit (debulking) sediment, and lose (infiltration) or entrain (dilution) water. Especially non-cohesive lahars (<3–5% clay-sized particles) are prone to such phase transitions, typically evolving from proximal debris flows to hyperconcentrated flows or muddy streamflows in distal reaches (Pierson & Scott, 1985).

Direct collection of quantitative data on lahar events is inherently difficult, and especially rare for large-scale syneruptive flows. Understanding of the principal physical and rheological characteristics of lahars benefits from observations of experimental studies (Iverson et al., 2010) and natural debris flows (McArdell et al., 2007; McCoy et al., 2012). Key features include a pulsating progression (Doyle et al., 2011; Iverson, 1997; McArdell et al., 2007), long-lived pore-fluid pressure in excess of hydrostatic values contributing to long runout distances (Iverson, 1997; Lube et al., 2009; McArdell et al., 2007), and topographically controlled erosion and entrainment leading to a several-fold increase of discharge and flow volume after initiation (Berger et al., 2010; Berti et al., 1999; Manville, 2004; McCoy et al., 2012; Pierson et al., 1990; Scott et al., 2005).

1.2 | Lahar modelling approaches

Incorporating the wide range of flow behaviours and the dynamic processes characteristic of lahars in runout analyses poses a challenging task, so that any theoretical model or practical simulation tool necessarily draws on physical and rheological simplifications of varying degrees. Different computer codes simulating lahars have been proposed, including the widely used empirical model LAHARZ (Iverson et al., 1998), which predicts inundation limits (Delaite et al., 2005; Huggel et al., 2008; Lee et al., 2015; Muñoz-Salinas et al., 2009; Pistolesi et al., 2014; Schneider et al., 2008; Worni et al., 2011), the cellular-automaton model LLUNPIY (Lupiano et al., 2020; Machado et al., 2015), and a variety of physically based numerical models that apply different rheology assumptions. Among these, 1-D models are today largely supplanted by multiscale continuum models with depth-averaged equations for conservation of mass and momentum. Among rheological laws, fluid dynamics-based models that propagate lahars as Newtonian flows are frequently applied. Such models (e.g. the dynamic flood-routing code Delft3D) can well reproduce dilute lake-breakout lahars from Mount Ruapehu, NZ (Carrivick et al., 2008). However, modelling lahars as Newtonian fluids neglects that lahars differ substantially in energy dissipation compared to typical Newtonian flood flows. Fluid-dynamic models may therefore be extended by the Manning's or Chézy's coefficient to approximate internal flow resistance. The hydraulic simulation software FLO-2D (O'Brien et al., 1993), designed for floods, mudflows and debris flows, uses the viscoplastic Bingham rheology model and encompasses flow resistance terms for yield, viscous, turbulent and dispersive stresses. Flo-2D is one of the most widely used single-phase rheological models in lahar hazard analysis (Caballero and Capra, 2014; Worni et al., 2011), whereas other rheological approaches—such as the Voellmy model—have only been rarely applied, though it has been formulated for (and proven to be successful in) simulating various types of sediment-laden flows. More sophisticated, 3-D models based on the Coulomb mixture theory (Iverson & Denlinger, 2001) describe a two-phase flow and the interactions between the solid and fluid phase. A simplified depth-averaged formulation of the mixture theory is incorporated in the simulation code Titian2D (Pitman & Le, 2005), and has been applied in a few studies for sediment-laden lahars (Procter et al., 2010; Williams et al., 2008).

With increasing model complexity and physical accuracy, a growing number of input parameters need to be defined, requiring appropriate material sampling and testing (Iverson & George, 2016). Complex models are also computationally expensive, restricting runout modelling to a specific, small section of the flow path (Procter et al., 2010). When modelling large-magnitude lahars over long distances, it is necessary to strike a balance between robustness and physical plausibility: computationally tractable, robust models are critical for application to large-scale drainage systems, while also capturing key flow features like stage heights, flow velocity, basal shear pressure, travel times, confluence, bifurcation and run-ups. Therefore, the numerical simulation software RAMMS for debris flow is chosen in this study, as it provides a good combination of simplification and physical plausibility and allows the tracing of sediment-laden lahars at Cotopaxi along the entire trajectory in large catchments.

1.3 | Erosion in lahar models

Entrainment of eroded material into the flowing mass can have a significant impact on flow propagation (Iverson, 1997; McDougall &

Hungr, 2005) and should therefore be considered in runout modelling and hazard assessment (Frank et al., 2015; Iverson & Ouyang, 2015). Although there is no common opinion on whether entrainment of substrate material reduces or enhances flow mobility (Iverson et al., 2011; Mangeney, 2011; Pudasaini & Fischer, 2016), an increase in flow volume has been observed to positively correlate with peak discharge, potential inundation area, runout distance, flow height and velocity (Rickenmann, 1999). The number of numerical models capable of simulating entrainment of mass flows is currently growing (Iverson & Ouyang, 2015), and the performance of the underlying theories is increasingly tested and validated against real mass flow events (Dietrich & Krautblatter, 2019; Frank et al., 2017; Hungr & McDougall, 2009; Hussin et al., 2012). The simulation of entrainment processes either requires the input of user-specific growth rates or of process-based erosion rates as a function of velocity (Fagents & Baloga, 2006) or shear stress (Frank et al., 2015; Iverson, 2012). Although lahars develop a considerable erosive force related to flow height, flow density and shear stress, lahar models have only rarely addressed erosional processes or volumetric changes (Carrivick, 2007; Carrivick et al., 2010; Fagents & Baloga, 2006; Lupiano et al., 2020), largely due to the shortcomings of the models used. These models are forced to start the calculation already with the hypothetical total flow volume, either on the volcano edifice or in channelized topography further downstream. This approach may not only lead to an overprediction of flow discharge and stage height, but also means that the dynamic evolution of syneruptive lahars, characterized by initial flow acceleration, rapid volumetric growth on the steep volcano flanks, and further erosion and deposition during downstream propagation, cannot be traced in the modelling process. Previous simulations for lahars from Cotopaxi using 1-D or 2-D flood-routing models (Aguilera et al., 2004; Barberi et al., 1992; Toapaxi et al., 2019; Vera et al., 2019) demonstrate the fluid-mechanical component applicable in the distant channels but not applicable to the initial runoff on the steep volcano flanks. Simultaneously, Ordóñez et al. (2013) and Pistolesi et al. (2014) estimated inundation areas with LAHARZ (Ordóñez et al., 2013; Pistolesi et al., 2014) but could not reproduce initial lahar formation because the model neglects dynamic bulking processes on the volcano flank. Lupiano et al. (2018) included glacier melting and erosion processes of syneruptive lahars from Cotopaxi with the use of LLUNPIY, but there the model is not calibrated and validated to an historic event using reproducible constraints.

1.4 | Aims of this study

This study aims to systematically assess the hazards of massive syneruptive lahars at Cotopaxi volcano in the densely inhabited northern and southern drainage system, by back-analysing the destructive 1877 lahar event, objectively constraining best-fitting model inputs and employing these for potential future lahars. Therefore, we (i) test the applicability of a Voellmy–Salm model for massive syneruptive lahars, (ii) develop a generic model simulating the lahar from the initiation on steep volcano flanks to the distal reaches, and (iii) include erosivity and entrainment on the steep slopes of a volcano edifice and along the trajectory in the generic model.

2 | STUDY SITE

2.1 | Geological setting and volcanic history

Cotopaxi is a large stratovolcano located in the Ecuadorian Andes of South America, ~60 km southeast of Quito, Ecuador's capital (Figure 1). The volcanic edifice stands on the metamorphic belt corresponding to the Cordillera Real, but is also partially interbedded with volcanic formations from the neighbouring Chalupas Caldera (Hall & Mothes, 2008). The glacier cap of the Cotopaxi extends from its summit (5897 m a.s.l.) down all the flanks, reaching ~4900 m a.s.l. on the eastern flank and ~5300 m a.s.l. on the western flank. Similar to other tropical glaciers of South America, Cotopaxi's glacier cap has been retreating rapidly for several decades (Cáceres, 2017; Vuille et al., 2018).

The geological evolution of Cotopaxi started with an ancient complex named Cotopaxi I between 560 and 420 ka BP, followed by a long period of quiescence (Hall & Mothes, 2008). The volcano resumed its activity around 13 ka BP with the formation of the current edifice Cotopaxi II, which is characterized by andesitic and rhyolitic eruptions. Around 4.5 ka BP, the last rhyolitic eruption took place and produced the partial collapse of the northern volcano flank, with subsequent formation of a debris avalanche and a gigantic cohesive lahar (Mothes et al., 1998).

The last 2100 years at Cotopaxi II have witnessed repetitive andesitic eruptions characterized by the deposition of lava flows, regional tephra layers and large-scale syneruptive lahars (Pistolesi et al., 2011, 2013). Average recurrence periods between 117 and 147 years may be estimated for Cotopaxi eruptions (Barberi et al., 1995), though it has been shown that the occurrence of eruptions displays significant clustering (Pistolesi et al., 2011).

Primary lahars formed during explosive eruptions undoubtedly represent the most hazardous phenomena at the Cotopaxi (Mothes et al., 2016; Pistolesi et al., 2013; Sierra et al., 2019). These flows are formed during explosive eruptions, when pyroclastic density currents move on top of the volcano glacier and melt it, instantaneously producing large volumes of water quickly mixing with volcanic rocks (Pistolesi et al., 2013). These flows transit through the three main drainage systems descending from the volcano (Figure 1): Rio Pita to the north, Rio Cutuchi to the south, and Rio Tambo to the east. All three drainages are characterized by alternations of deep, steep-gradient canyons that channel the flows, with wide, flat areas where significant deposition occurs (Mothes et al., 2004). Rio Pita and Rio Cutuchi transit the densely inhabited zones of Quito and Latacunga, respectively (Mothes et al., 2016), while Rio Tambo reaches the sparsely populated Amazonian basin (Sierra et al., 2019).

The most recent volcanic activity at Cotopaxi was recorded in April 2015 and identified by the monitoring system (Hidalgo et al., 2018). The anomalous records increased steadily until mid-August, when hydromagmatic activity started, producing significant ash venting from the summit crater (Bernard et al., 2016; Gaunt et al., 2016). This activity decreased progressively, waning in December

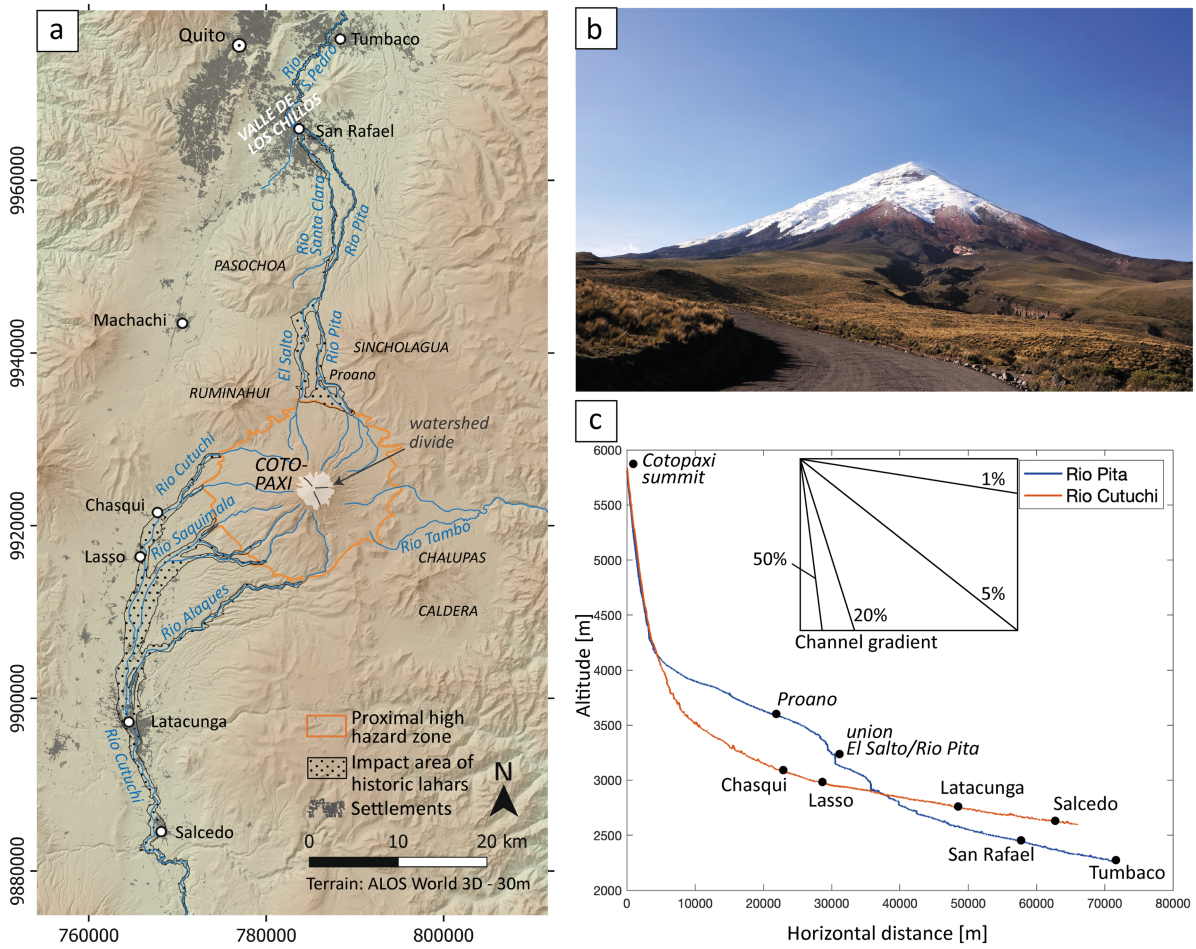

FIGURE 1 (a) Location of Cotopaxi volcano in Ecuador's Inter-Andean Valley and the surrounding major cities or settlements located along the drainages. The orange line delineates the proximal high-hazard zone around the volcano, the dotted area represents the inundation area of the 1877 lahar and other 18th-century lahars in the northern and southern drainage system (Mothes et al., 2016); lahars in the eastern drainage are not considered in this study. (b) View of the north flank of glacier-clad Cotopaxi volcano. (c) Longitudinal profiles of two major lahar channels, the Rio Pita (northern drainage) and Rio Cutuchi (southern drainage) [Colour figure can be viewed at wileyonlinelibrary.com]

2015 (Hidalgo et al., 2018), and did not produce syneruptive lahars.

2.2 | The 1877 lahar disaster

The last syneruptive lahar from Cotopaxi occurred on 26 June 1877. According to reports by Sodiro (1877) and Wolf (1878), Cotopaxi had been in eruption since early 1877, but in June its activity increased significantly. That day, the volcano produced a sustained explosive phase with widespread pyroclastic density currents descending all the edifice's flanks. Estimations by these authors suggest that the explosive eruption lasted at least 15 min, and that it took around 1 h for the lahar front to arrive in Latacunga (south) and the Chillos Valley (close to Quito to the north).

In the Pita drainage, the 1877 lahar experienced a significant runover, diverting ~20% of its volume into the Rio Santa Clara (Mothes et al., 2004), which transits densely populated areas in the Chillos Valley. The pirating effect occurred in the site called 'La Caldera', where the Rio Pita is deeply incised and experiences a sharp bend, while the headwaters of the Rio Santa Clara are placed just above. Calculations by Mothes et al. (2004), assuming that the pirating effect was produced by overflowing resulting from super-elevation in a forced vertex, suggest that the discharge rate was >40 000 m^3/s, but they also suggest that the flow could have been partially dammed by the very narrow canyon immediately downstream.

The lahar deposit from 1877 can still be distinguished in the landscape of the proximal north and north-eastern lower flanks of Cotopaxi: it contains a specific type of scoriaceous volcanic bomb with a unique feature of fracturing and disaggregating easily when hit lightly with a hammer (Mothes et al., 2004), which was not repeated in volcanic bombs from 18th-century lahar deposits. This enables detailed mapping of the deposits, especially in the proximal zones (<20 km from the source), as well as measurement of precise cross-sections from which physical parameters like height, velocity and discharge rate may be obtained (Aguilera et al., 2004; Mothes et al., 2004). Total lahar volumes are estimated to be about 60–75 × 10^6 m^3 in the northern drainage and about 80–100 × 10^6 m^3 in the southern drainage, respectively (Mothes et al., 2004).

The 1877 lahar was influenced by the morphology of the transited channels (Mothes et al., 2004). In the northern and southern drainages, the flows initially transit the deep canyons of the volcanic edifice with assumed erosive behaviour. A first zone of deposition occurs in flat regions at the foot of the volcano. Afterwards, zones of erosion and/or energy increase alternate with flat regions. Granulometric characteristics of the 1877 deposits vary between

those of debris flows and hyperconcentrated flows, with proximal samples (<40 km from source) displaying granular debris flow distributions, while distal ones (up to 70 km from source) show rather hyperconcentrated characteristics (Mothes et al., 2004; Pistolesi et al., 2013). Deposits from the 1877 lahar are granulometrically similar to other deposits from Cotopaxi eruptions in the 18th century and lack significant amounts of very fine-grained, clay-sized particles (Mothes et al., 2004), as is characteristic of non-cohesive flows.

3 | METHODS

3.1 | RAMMS model

We apply the physically based dynamic model RAMMS, which is widely used in runout modelling of different types of mass movements including snow avalanches, rock avalanches, debris flows and GLOFS (Frey et al., 2018; Hussin et al., 2012; Schneider et al., 2010). The RAMMS debris flow model is formulated as a single-phase system that propagates the solid–fluid mixture as an incompressible bulk flow with mean constant density (Bartelt et al., 2017; Christen et al., 2010). It requires careful calibration of the two governing frictional parameters of the Voellmy–Salm rheology and delivers information on key parameters for hazard assessment, such as runout distance, height and velocity of the flow, impact pressure, erosion and deposition. The core of the program is a second-order numerical solution scheme to solve the depth-averaged equations of motion in 3-D terrain (x,y,z) at time t (Christen et al., 2010). The mass balance is given by

$$\dot{Q}(x,y,t) = \partial_t H + \partial_x(HU_x) + \partial_y(HU_y) \tag{1}$$

where $\dot{Q}(x,y,t)$ denotes the mass production source term, $H(x,y,t)$ the flow height and $U(x,y,t)$ the depth-averaged velocity. The depth-averaged momentum balance in the x and y directions is given by

$$\partial_t(HU_x) + \partial_x\left(HU_x^2 + g_z k_{a/p}\frac{H^2}{2}\right) + \partial_y(HU_xU_y) = S_{gx} - S_{fx} \tag{2}$$

and

$$\partial_t(HU_y) + \partial_y\left(HU_y^2 + g_z k_{a/p}\frac{H^2}{2}\right) + \partial_x(HU_xU_y) = S_{gy} - S_{fy} \tag{3}$$

respectively, where $g = (g_x, g_y, g_z)$ describes the gravitational vector, $k_{a/p}$ is the earth pressure coefficient (normally set to 1), S_g and S_f denote the slope parallel gravitational acceleration and frictional deceleration, respectively.

The frictional resistance S_f is described using a Voellmy–Salm approach (Salm, 1993; Voellmy, 1955), which incorporates a dry Coulomb friction μ proportional to the normal stress and a velocity-squared drag or viscous-turbulent friction ξ (similar to Chézy friction) (Bartelt et al., 1999; Christen et al., 2010; Fischer et al., 2012):

$$S_f = \mu N + \frac{\rho g U^2}{\xi} \quad \text{with} \quad N = \rho H\left[g\cos(\varphi) + \kappa U^2\right] \tag{4}$$

where ρ is the density of the mass, φ the slope angle of the surface, and κ the terrain curvature in the flow direction. The Coulomb friction μ accounts for the resistance of the solid phase, is independent of velocity, and governs flow behaviour when moving slowly, while the turbulent friction ξ accounts for the fluid phase, scales with flow velocity, and dominates at higher velocities in acceleration zones (Bartelt et al., 2017; Christen et al., 2010).

An implemented entrainment module in RAMMS predicts the depth of erosion in terms of net decrease in elevation of the channel bed (Frank et al., 2017). It simulates the increase in flow volume due to entrainment (Frank et al., 2017), but sediment entrainment is not coupled to topographic changes in the underlying digital elevation model (DEM) or changes in flow behaviour. Field observations at the exceptionally active Illgraben catchment in Switzerland on erosion depths (Schürch et al., 2011) and erosion rates (Berger et al., 2011) of naturally occurring debris flows served as the basis for the development of the entrainment algorithm (Frank et al., 2015). The potential erosion depth e_m per grid cell is described as a function of the computed shear stress acting on the channel bed, given by

$$\tau = \rho g H \sin\varphi \tag{5}$$

and is related to a critical shear stress τ_c and a proportionality factor $\frac{dz}{d\tau}$ controlling the rate of vertical erosion, given by

$$e_m = \begin{cases} 0 & \text{for } \tau < \tau_c \\ \dfrac{dz}{d\tau}(\tau - \tau_c) & \text{for } \tau \geq \tau_c \end{cases} \tag{6}$$

Based on average erosion rates recorded at the Illgraben (Berger et al., 2011), a specific erosion rate $\frac{dz}{dt}$ is used (Frank et al., 2015):

$$\frac{dz}{dt} = -0.025 \quad \text{for} \quad e_t \leq e_m \tag{7}$$

Sediment entrainment starts once the critical shear stress τ_c is exceeded, and ends when the actual erosion depth e_t reaches the maximal potential erosion depth e_m. Specified variations of the erosion parameters are described in the model calibration section below, and further details of the RAMMS model and the implemented entrainment model are available in Christen et al. (2010) and Frank et al. (2015, 2017).

3.2 | Model setup

We aim to set up the RAMMS lahar model in a generic way by starting the flow on the volcano flank close to the crater, enabling sediment bulking along the path and propagating the lahar until distal reaches. The setup is designed for the purpose of back-calculating the 1877 lahar event and can be applied to forward modelling of potential future lahars.

3.2.1 | Model premises: DEM and limits of model domain

Lahars from Cotopaxi usually do not show coherent deposit limits but may travel up to 325 km, as reported for the 1877 lahar (Mothes et al., 2004), distally in a watery phase. Therefore, the modelling region is restricted by the largest urban centres around the volcano:

to the north, the model region extends until approximately 70 km downstream of the volcano, covering the urban agglomeration of Valle de Los Chillos; to the south, it ends south of the city of Salcedo about 65 km downstream of Cotopaxi (see Figure 2). Given the large extent, a spatial resolution of 10 m is considered sufficient for capturing key flow patterns. All numerical simulations conducted in this study are based on a 10 m DEM, which we resampled from an original 4 m-resolution DEM developed by the SIGTIERRAS project in 2010 (Ministerio de Agricultura, Ganadería, Acuacultura y Pesca). No detailed information is available on valley morphology before the 1877 lahar passage. However, we can assume that the present-day topography of the partly deeply incised major channels does not differ significantly, because historical and stratigraphic evidence suggests that they confined all known historic lahars since the 18th century (Hall & Mothes, 2008).

3.2.2 | Model premises: Erosion and entrainment

We are aware of the high uncertainties involved with modelling lahar erosivity, as no quantitative information exists about the erosion potential of historic lahars at Cotopaxi. Alternatively, by neglecting dynamic bulking and debulking, it would be necessary to already start the model with the total lahar volume, which may lead to an overestimation of peak discharge and flow height (Frank et al., 2015). Our approach to simulate sediment entrainment along the trajectory is therefore (i) focused on modelling the overall mass balance and reproducing averaged total flow volumes reported by Mothes et al. (2004) and (ii) based on a straightforward characterization and mapping of substrate erodibility. We use orthophotographs taken in 2011, 2014 and 2016, provided as WMS by IGM Ecuador, topographic as well as geological maps (Hall & Mothes, 2008; Vezzoli et al., 2017) for a straightforward characterization of substrate erodibility related to lithology (bedrock/soil) and consolidation, which we cross-checked at critical locations in the field.

Three erosion classes can be defined based on the erodibility of the substrate. We assign (1) the RAMMS default entrainment settings (average values derived from measurements at the Illgraben catchment) along most of the lahar-affected channels in the valleys, where deposits of numerous historical lahars and scoria flows prevail. Additionally, we discriminate between (2) areas with comparatively higher erodibility located on the volcano flank, where

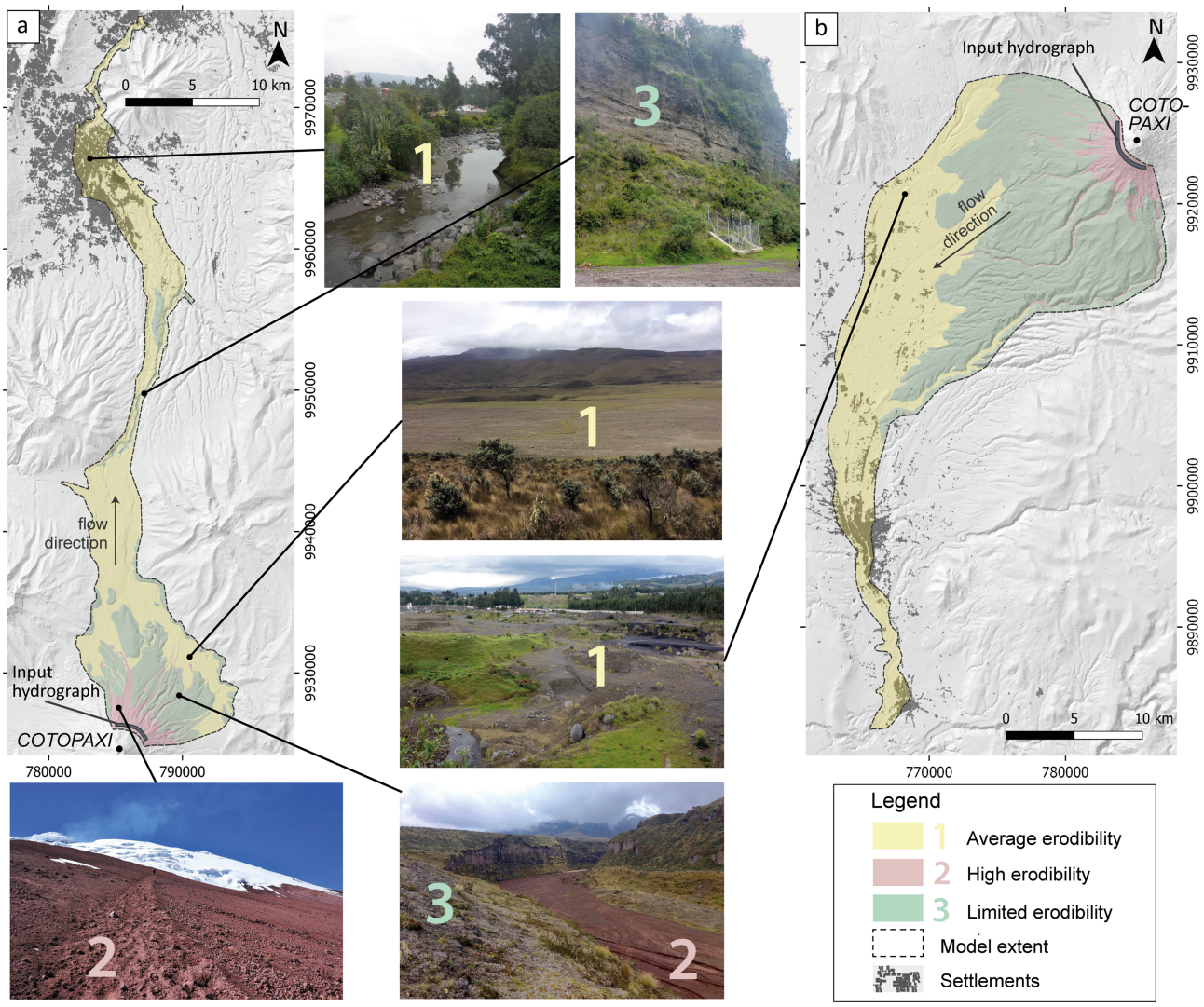

FIGURE 2 Spatial distribution of the erosion classes within the northern (a) and southern (b) model region. The classification is based on estimates of substrate erodibility, supported by geomorphological and lithological features. The photographs provide examples of each erosion class [Colour figure can be viewed at wileyonlinelibrary.com]

abundant loose, pyroclastic sediment or glacial deposits exposed by recent glacier retreat are present, and (3) areas with limited erodibility characterized by regolith-covered bedrock, or deep bedrock-flanked channels.

For each class, we specify the RAMMS entrainment parameters that control the degree of sediment entrainment into the flow (Table 1) from a set of given values (Bartelt et al., 2017; Frank et al., 2015, 2017). In areas with 'limited erodibility', the maximum erosion depth is constrained to 0.5 m modulated by assumed regolith thickness, whereas areas with 'average' and 'high erodibility' are considered supply-unlimited.

3.2.3 | Estimation of initial volume and input hydrograph

Estimations of the volume and peak discharge of mass flows are critical baseline information for modelling. For back-calculating the 1877 lahar, we reproduce the average of total volumes reported by Mothes et al. (2004) (i.e. $\sim 68 \times 10^6$ m^3 for the northern and $\sim 90 \times 10^6$ m^3 for the southern drainage, respectively). The desired flow volumes are achieved by a stepwise approximation balancing the sum of input and eroded volumes. We iteratively test input volumes between 25×10^6 and 58×10^6 m^3 and analyse the resulting dynamic volumetric growth of the lahar. Within this model series, the friction parameters are kept constant at μ = 0.01 and ξ = 1800 m/s^2 (taken from the core of the sensitivity matrix), but we expect that especially changing μ may affect modelled erosion volumes, as reported by Frank et al. (2015). In comparison to the total volumes of the simulated flows, this may only have a minor effect.

For a rough approximation of the release hydrograph, we use an idealized three-point discharge hydrograph. The shape parameters draw upon the following empirical relation and observations:

1. *Peak discharge*. Mizuyama et al. (1992) proposed an empirical formula to estimate the peak discharge Q_p of granular debris flows as a function of volume V, given by

$$Q_p = 0.135V^{0.78} \quad (8)$$

Pierson (1998) tested the applicability of this correlation for large-magnitude lahars and found that it serves as an adequate approximation for near-source peak discharges. The formula is applied to the tested initial lahar volumes ranging from 25×10^6 to 58×10^6 m^3.

2. *Time of peak discharge*. Well-studied lahars at the glacier-capped volcanoes of Mount St. Helens and Nevado del Ruiz showed a relatively instantaneous release of flow (Pierson, 1995; Pierson & Scott, 1985; Pierson et al., 1990). The time of peak discharge is therefore set to 120 s after initiation.
3. *Duration*. We can conservatively consider eyewitness accounts of pyroclastic flow duration as a proxy for the duration of lahar release. Wolf (1878) reported that pyroclastic flows lasted for 15–20 min and caused immediate melting of snow and ice all over the crater. Application of the above-described volume–discharge correlation by Mizuyama et al. (1992) to a triangular-shaped hydrograph yields release durations of about 12 min, which is largely in accordance with eyewitness observations.

One broad release hydrograph is placed at the upstream boundary of each of the two river systems, near the present location of the glacier snouts. This enables the injected flow to drain completely into one system, and all major channels of the respective drainage system are affected simultaneously.

3.3 | Model calibration and sensitivity analysis

We back-calculate the well-documented 1877 lahar event in the northern drainage system of Cotopaxi in order to evaluate the performance of the model and to derive plausible model parameter values for future lahar scenarios. All available information on the reference event is based on eyewitness reports by Sodiro (1877) and Wolf (1878), official hazard maps provided by IG-EPN of Ecuador (Mothes et al., 2016), and sedimentological field investigations by Mothes et al. (2004). In total, 14 calibration criteria are selected (Figure 3), encompassing different types of rheological parameters and a representative spatial distribution along the lahar path. We differentiate between two categories for calibration criteria on the basis of data reliability:

- 'Primary criteria' include those which any realistic lahar model back-calculating the 1877 lahar must have: (i) the lahar flowed over the northern channel wall at La Caldera (corresponding to flow height > 42 m given by the used DEM), (ii) in consequence it inundated the town of Sangolquí, and (iii) also reached Tumbaco further downstream in a reasonable time.
- 'Additional criteria' comprise less reliable rheological data, such as eyewitness observations on arrival times at locations downstream, and estimates on flow velocity, peak discharge, stage heights and inundation limits derived from field investigations more than 100 years after the event. The official hazard map of IG-EPN (Mothes et al., 2016) delimits potential lahar inundation areas for lahars triggered by moderate to strong eruptions, based on field mapping of deposits of the 1877 lahar and other 18th-century lahars.

TABLE 1 Model parametrization for the three different erosion classes

Erosion class	Erosion rate [m/s]	Potential erosion depth [kPa^{-1}]	Yield stress [kPa]	Maximum erosion depth [m]
(1) Average erodibility	0.025	0.1	1.0	–
(2) High erodibility	0.05	0.2	0.5	–
(3) Limited erodibility	0.013	0.05	1.5	0.5

The calibration criteria act as simulation constraints and are used to determine best-fit input parameter combinations. Because input parameters may cause a significant change in the model's behaviour, we systematically analyse the sensitivity of the two Voellmy–Salm friction coefficients μ and ξ, the flow density, and the initial velocity to model outcomes for runout distance, peak discharge, travel time, flow velocity and flow height (represented by the calibration criteria).

Given the location of the release hydrographs at least 1000 m downslope of the crater, the lahar most likely has already started to evolve due to melting of glacier ice and mixing with freshly ejected volcanic products upon 'arriving' at the location of the release hydrograph. It seems likely that the initial flow has already accelerated to a certain velocity, which is approximated by exploring the initial velocity between 10 and 20 m/s in steps of 5 m/s. The density of the modelled flow is varied in 200 kg/m^3 increments from 1400 to 2200 kg/m^3, representing known densities of hyperconcentrated flows and debris flows. According to calibrated Voellmy friction coefficients for debris flows and GLOFs in previous studies (Frey et al., 2018; McDougall, 2006; Revellino et al., 2004; Schneider et al., 2014; Schraml et al., 2015), the parameter space may span a wide range from 0.01 to 0.2 for μ values and from 200 to 1500 m/s^2 for ξ values, with a tendency for lower μ and higher ξ for large-magnitude flows. Here, we vary the μ coefficient from 0.0025 to 0.05, with steps of 0.0025 between 0.0025 and 0.01, and steps of 0.005 between 0.01 and 0.05. The ξ value is varied between 600 and 3000 m/s^2 in increments of 400 m/s^2.

3.4 | Evaluation of model performance

In order to objectively evaluate the quality of model predictions with RAMMS, we separately compare model outcomes (m_i) to target values (t_i) for calibration measures (i) of flow velocity, flow height, travel time and peak discharge. The performance of a simulation (ϕ) using a given set of input parameters (y) is quantified as percentage deviation, with

$$\phi_i(y) = \frac{m_i(y) - t_i}{t_i} \cdot 100 \quad (9)$$

Normalizing the differences between modelled and targeted values facilitates an easy comparison between the different rheological measures of the calibration criteria.

Similarity between simulated and mapped lahar impact area (cf. Figure 3) is expressed as percentage overlap, dividing the number of grid cells correctly modelled as inundated (true positives) by the total number of modelled cells (true positives + false negatives). It does not seem meaningful to include false positives in this case, because the mapped lahar impact area encompasses inundation limits

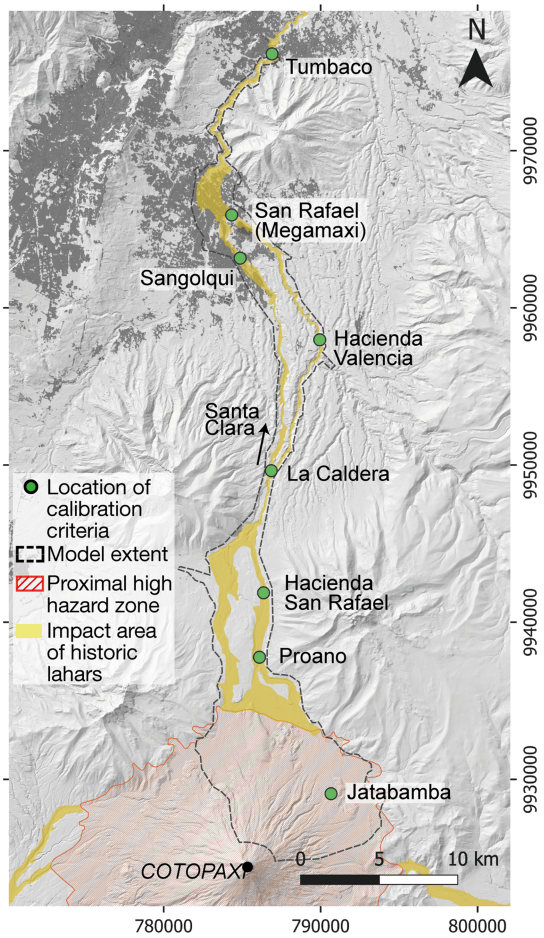

Location	Calibration measure	Target value	Reference
Primary Criteria			
La Caldera	Height	> 42 m (overflow to Sta. Clara)	Height from DEM; Sodiro (1877), Wolf (1878)
Sangolquí	Inundation by lahar	-	Sodiro (1877), Wolf (1878)
Tumbaco	Lahar passage	-	Sodiro (1877)
Additional Criteria			
Inundation map of 1877 and historic lahars			Mothes et al. (2016)
Jatabamba	Velocity	18 m/s	Mothes et al. (2004)
Proano	Velocity	20 m/s	Mothes et al. (2004)
Proano	Peak discharge	49,000 m³/s	Mothes et al. (2004)
Hacienda San Rafael	Height	27 m	Mothes et al. (2004)
Hacienda San Rafael	Velocity	20 m/s	Mothes et al. (2004)
La Caldera – Sta. Clara	Peak discharge	14,000 m³/s	Mothes et al. (2004)
Sangolquí	Travel time	< 1 h	Sodiro (1877)
Hacienda Valencia	Height	15 m	Mothes et al. (2004)
San Rafael (Megamaxi)	Height	12 m	Mothes et al. (2004)
Tumbaco	Travel time	1.5 h	Sodiro (1877)

FIGURE 3 Summary of all 14 calibration constraints used for back-calculating the 1877 lahar event, categorized into 3 'primary' and 11 'additional' calibration criteria. Locations of the calibration constraints along the northern runout path are shown on the map on the left; the inundation limits are derived from Mothes et al. (2016) [Colour figure can be viewed at wileyonlinelibrary.com]

of the 1877 lahar but also of several other historic lahars. The calculation is applied to the shared extent of both layers (i.e. neglecting the proximal zone around the volcano) and considers simulated impact areas inundated by more than 0.05 m. To harmonize model outcomes, the results are further depicted as model deviation (100 – percentage overlap).

For each set of input parameters (y), the values of the constraint-wise performance analyses are then summed to give a single simulation performance value (ϕ_{total}), with

$$\phi_{total}(y) = \frac{\sum_{i=1}^{n} \left| \left(\frac{m_i(y) - t_i}{t_i} \cdot 100 \right) \right|}{n} \quad (10)$$

This number highlights minimum model deviations within the analysed input parameter space and thereby allows us to select the most representative parameter combinations for the back-calculated event.

3.5 | Simulation of potential future lahars

Based on investigations about the eruptive history of Cotopaxi (Hall & Mothes, 2008; Mothes et al., 1998, 2004), Andrade et al. (2005) proposed four potential future eruption scenarios (Figure 9a), which can be linked to the size of the eruption expressed as Volcanic Explosivity Index (VEI) (Newhall & Self, 1982): the weakest expected eruption (VEI 1–2) is characterized by Strombolian activity, small to moderate tephra emissions and ejection of ballistic projectiles, whereas during eruptions of VEI 2–3, VEI 3–4 and VEI > 4 with Vulcanian-, sub-Plinian- and Plinian activity, respectively, the eruption is most likely accompanied by pyroclastic flows. Because pyroclastic flows are necessary agents to melt significant amounts of snow and ice required for the generation of syneruptive lahars, the hypothetical lahar Scenario 1 is here excluded from runout modelling. For comparison, during the last eruption at Cotopaxi in 2015, classified as VEI 1–2 (Mothes et al., 2017), no syneruptive lahar but instead several small-scale secondary lahars occurred inside the proximal zone. An increase in VEI likely corresponds to larger volumes and dispersal of emitted tephra, and increasing energy and spatial impact of pyroclastic flows (Andrade et al., 2005). A VEI 3–4 scenario, equivalent to the 1877 eruption, may be characterized by a 'boiling-over' activity producing scoria flows, whereas during highly explosive VEI > 4 Plinian eruptions, a collapse of the eruption column can affect the entire summit glacier (Pistolesi et al., 2013). Previous studies have therefore concluded that a larger degree of volcano-glacier interactions with increasing VEI results in more voluminous and destructive potential lahars (Mothes et al., 2004; Ordóñez et al., 2013; Pistolesi et al., 2013).

A common, but simplified approach to estimate lahar volumes at Cotopaxi (Barberi et al., 1992; Mothes et al., 2004; Ordóñez et al., 2013;Toapaxi et al., 2019 ; Vera et al., 2019) relies on three controls: the two dynamic controls include (i) variable thicknesses of ice and snow melted uniformly from the glacier surface during an eruption as a proxy for the degree of volcano-glacier interactions, and (ii) the size of the summit glacier. A third, static control for estimation of total lahar volume is (iii) the assumption of a threefold volume growth of the lahar due to incorporation of solids. Scaling of melted ice thickness between the scenarios has been realized with a factor of approximately 2, assuming a uniform melting of respectively 2, 4–5 and 8–10 m for an eruption of VEI 2–3, VEI 3–4 and VEI > 4. Regarding the extent of Cotopaxi's glaciers, Cáceres (2017) reported that the surface area has diminished on average by about 52% between the years 1977 and 2016. With the calculation of lahar volumes being based on the melting thickness and the glacier extent, a glacier retreat of about 50% would directly translate into a 50% reduction in initial volumes of potential future lahars compared to the situation during the 1877 eruption (Toapaxi et al., 2019; Vera et al., 2019).

We adapt some of these simplified assumptions to the quantification of future lahar scenarios in this study by using the following approach:

1. The calibrated lahar model of the 1877 eruption with estimated release discharge and input volume (defining the input hydrograph) provides the basis for scenario modelling. The modelled event was equivalent to a VEI 3–4 eruption.
2. Due to a 50% reduction in glacier surface area, a future VEI 3–4 eruption is expected to produce lahars with release discharges half those of the 1877 lahar (assuming that the total glacier areas in 1877 and 1977 were of the same extent). This clearly represents a simplified assumption; the degree to which glacier retreat affects future lahar magnitudes may also need a closer look at eruption dynamics and triggering mechanisms (Pistolesi et al., 2013, 2014), as discussed later.
3. A scaling factor of 2 is used to express the increasing degree of volcano-glacier interactions with increasing VEI. Proceeding from a VEI 3–4 scenario, we halve the release discharges for future VEI 2–3 events, and double them for future VEI > 4 scenarios. The according input volumes are estimated using the discharge–volume relation of Mizuyama et al. (1992) (Equation 8).
4. The initial lahar can dynamically change its volume due to entrainment and deposition of material. Erosion of the flow is controlled by the erodibility of the substrate.

4 | RESULTS

4.1 | Estimation of input volume, entrained volume and input hydrograph for the 1877 lahar

Analysis of model input volumes for back-calculating the 1877 lahar was started in the northern and southern drainage with an initial volume guess of 25×10^6 m^3, but as the modelled total flow volumes were too low, input volumes were raised to 34×10^6 m^3 and successively increased by increments of 3×10^6 m^3. Targeted total flow volumes ($\sim 68 \times 10^6$ m^3 in the northern and $\sim 90 \times 10^6$ m^3 in the southern drainage) are well approximated with an input volume of 46×10^6 m^3 in the northern and 49×10^6 m^3 in the southern drainage, respectively (Figure 4). By applying these values in the volume–discharge equation given by Mizuyama et al. (1992) (Equation 8), we obtain peak discharges of 128 000 m/s^3 in the northern and 134 500 m/s^3 in the southern drainage. In this way, all shape parameters defining the three-point release hydrograph are estimated.

Given the entrainment settings (Figure 2 and Table 1), a flow with an initial volume of 46×10^6 m^3 erodes and entrains about 23×10^6 m^3 along its runout to the north, whereas in the southern drainage, an initial flow of 49×10^6 m^3 grows by 40×10^6 m^3 due to entrainment.

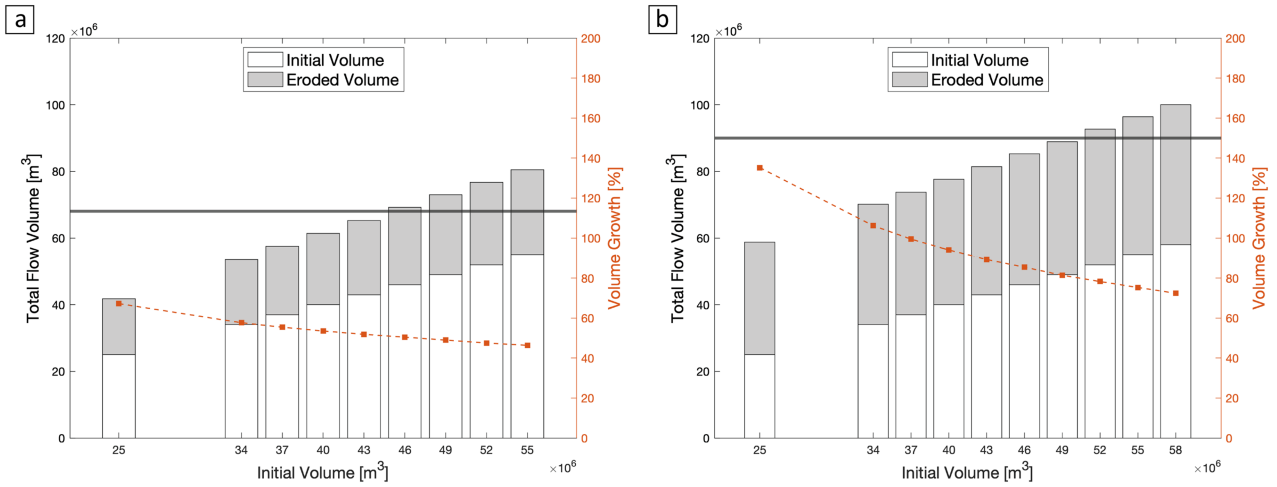

FIGURE 4 Iterative approximation of input volume (white) and accordingly modelled eroded volume (grey) in order to best estimate the input volume for simulating the 1877 lahar with target volumes (indicated as grey solid line) of ~68 × 10^6 m^3 in the northern (a) and ~90 × 10^6 m^3 in the southern drainage (b), respectively. The simulations are performed with μ = 0.01 and ξ = 1800 m/s^2 [Colour figure can be viewed at wileyonlinelibrary.com]

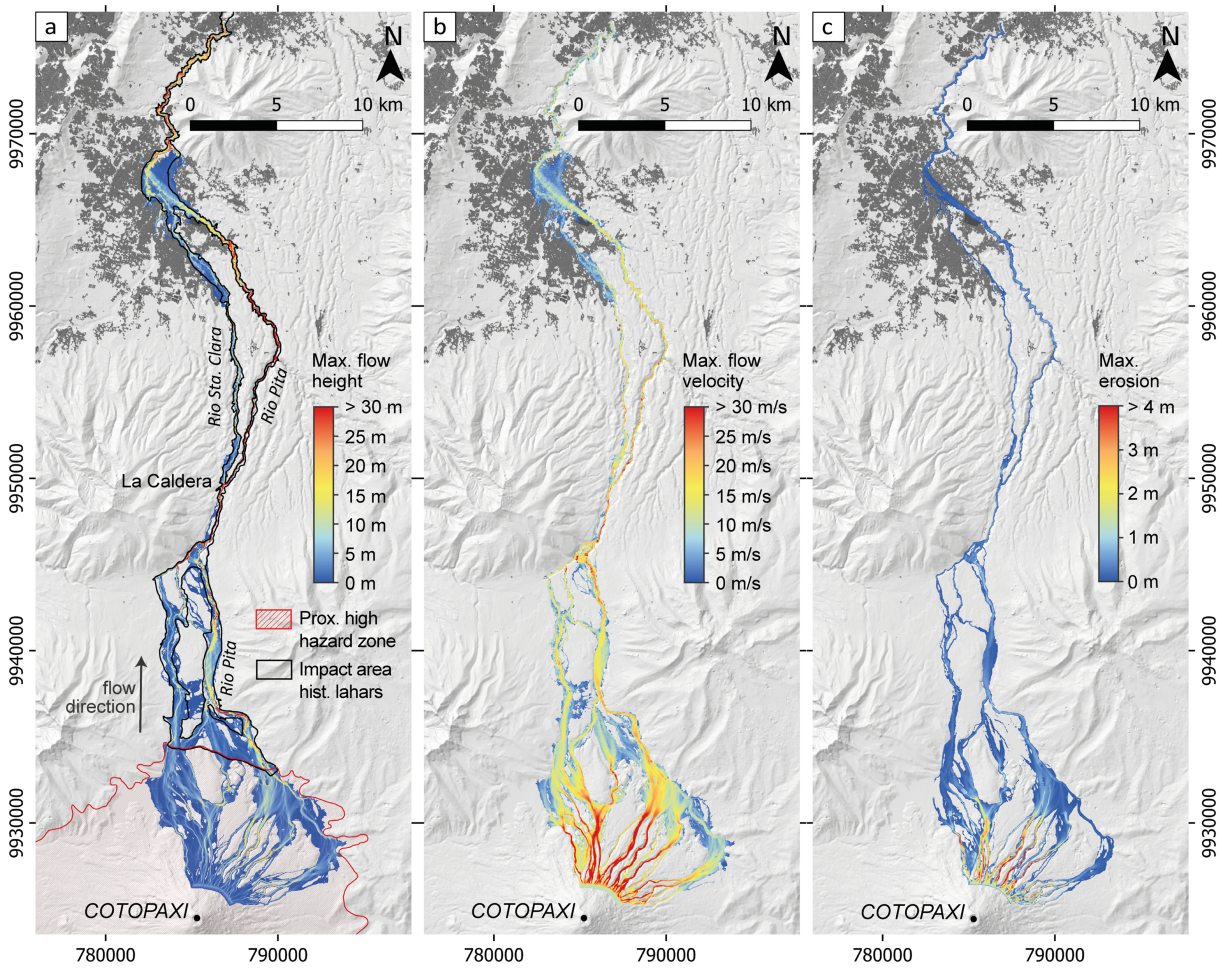

FIGURE 5 Back-calculated 1877 lahar in the northern sector based on calibrated input parameters with best fit for μ = 0.005 and ξ = 1400 m/s^2. Simulation results are illustrated for (a) maximum flow heights, compared to mapped lahar impact area of historical lahars (Mothes et al., 2016), (b) maximum flow velocity and (c) maximum erosion by the flow [Colour figure can be viewed at wileyonlinelibrary.com]

This corresponds to a volume growth of 50 and 80% in the northern and southern drainage system, respectively. At both river systems, we can observe that the amount of eroded material varies with initial volume, revealing a general trend towards smaller erosion-attributed volume growth with increasing input volume. This trend is more pronounced in the southern drainage, where erosion and entrainment results in a volume growth ranging from 135% for an initial volume of 25 × 10^6 m^3 to 70% for an initial volume of 58 × 10^6 m^3.

4.2 | Model calibration and sensitivity analysis

Within a series of pilot runs, we found that flow density and initial velocity only slightly affect flow propagation. Modifications of flow density result in model outcomes for arrival times (Sangolqui), flow heights (La Caldera) and peak discharges (Proano) differing by 5, 2 and 15%, respectively. A change in initial flow velocity leads to arrival times (Sangolqui), flow heights (La Caldera) and peak discharges (Proano) differing by 1, 0.4 and 4%, respectively. Based on these observations, we kept the flow density at a constant value of 2000 kg/m^3 and started all simulations with a velocity of 10 m/s. The sensitivity analysis was thus limited to the governing friction parameters μ and ξ of the Voellmy–Salm rheology.

First, we analysed whether model outcomes meet the required 'primary calibration criteria'. In simulations using μ > 0.02, the lahar does not experience the observed overflow at La Caldera to the Sta. Clara headwaters, and when using μ > 0.015, the lahar does not reach Tumbaco within a reasonable calculation time of 4 h. Consequently, we could largely constrain the parameter space for the sensitivity analysis to μ coefficients ranging between 0.0025 and 0.02 and ξ coefficients between 600 and 3000 m/s^2, resulting in a total of 42 different μ/ξ combinations. Even though model runs with μ = 0.02 do not meet the requirements of all 'primary model constraints', this value is still included to get a broader understanding of model behaviour.

Second, we used the 'additional calibration criteria' in order to analyse model sensitivity and find best-fit parameter combinations. The results of the 42 model runs for each criterion are summarized in Figures 6, 7 and 8, and presented in four different ways, showing (a) the sensitivity of the model outcome as a function of μ and ξ, (b) a statistical analysis grouping frequency of model outcomes, (c) a visual matrix of model outcomes, and (d) a visual matrix representing the performance of a simulation (ϕ) in terms of model deviation from target value. We refer to Figure 3 for localization of the subsequent calibration constraints along the northern drainage. The model results for velocity show that this measure is sensitive to both the μ and ξ coefficients, but the sensitivity to the friction coefficient μ is increased at the downstream locations Proano and Hacienda San Rafael. Overall, the simulations gave velocities that compare favourably to all three target velocities. Model outcomes for flow height demonstrate that this calibration measure is highly sensitive to variations of μ and largely insensitive to variations of ξ. However, all model results at the two distal locations Hacienda Valencia and San Rafael (Megamaxi) clearly overestimate the targeted values, which may be attributed to

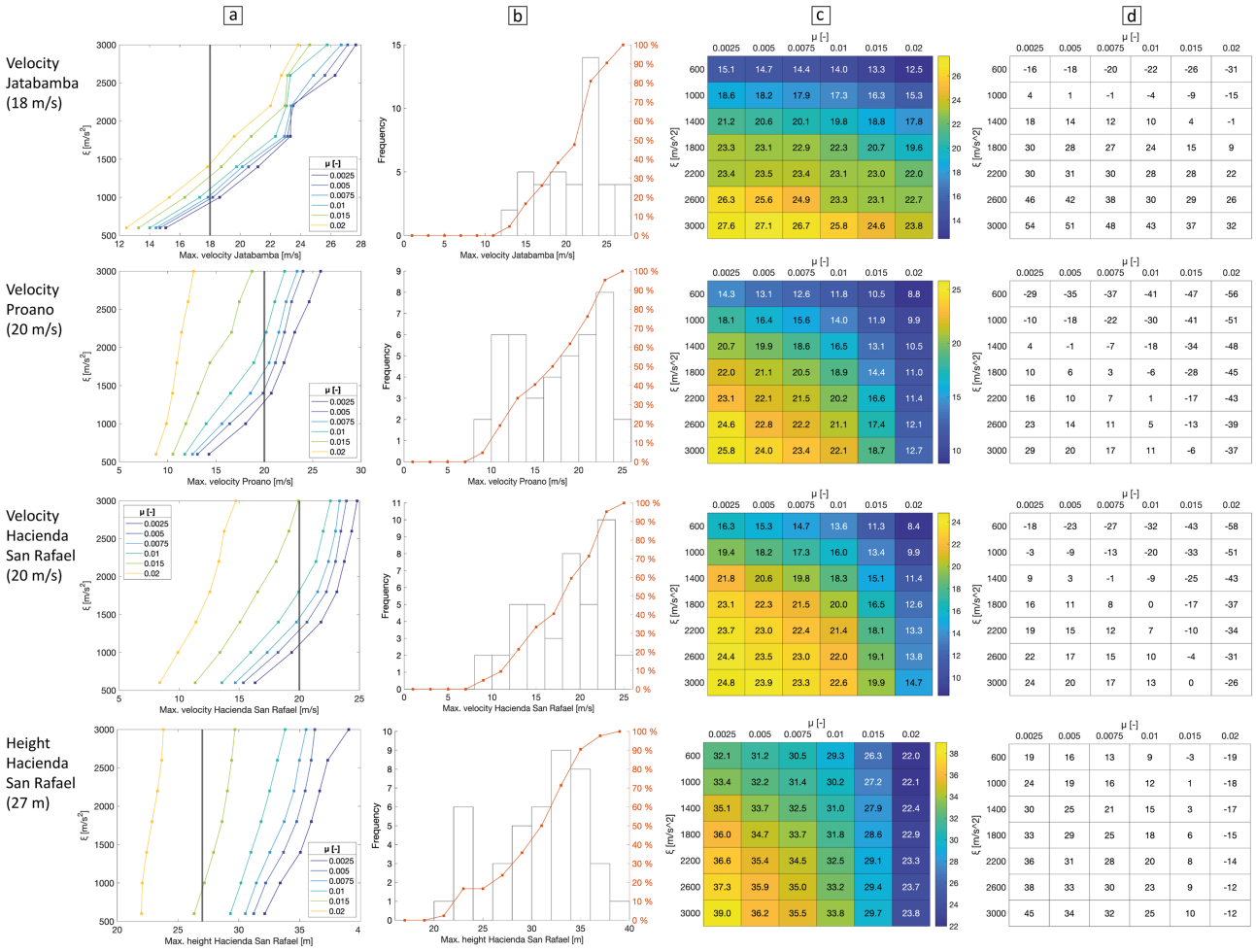

FIGURE 6 Model outcomes for calibration criteria for flow velocity and flow height. The target value of each criterion is given in brackets. (a) Sensitivity of the model outcome as a function of μ and ξ; (b) statistical analysis grouping frequency of model outcomes; (c) a visual, colour-coded matrix of model outcomes indicating increasing values of the considered measure from blue to yellow; (d) a visual matrix representing the performance of a simulation (ϕ) in terms of model deviation from target value. For each type of calibration measure (e.g. velocity), the calibration constraints are displayed in order of their distance to the volcano [Colour figure can be viewed at wileyonlinelibrary.com]

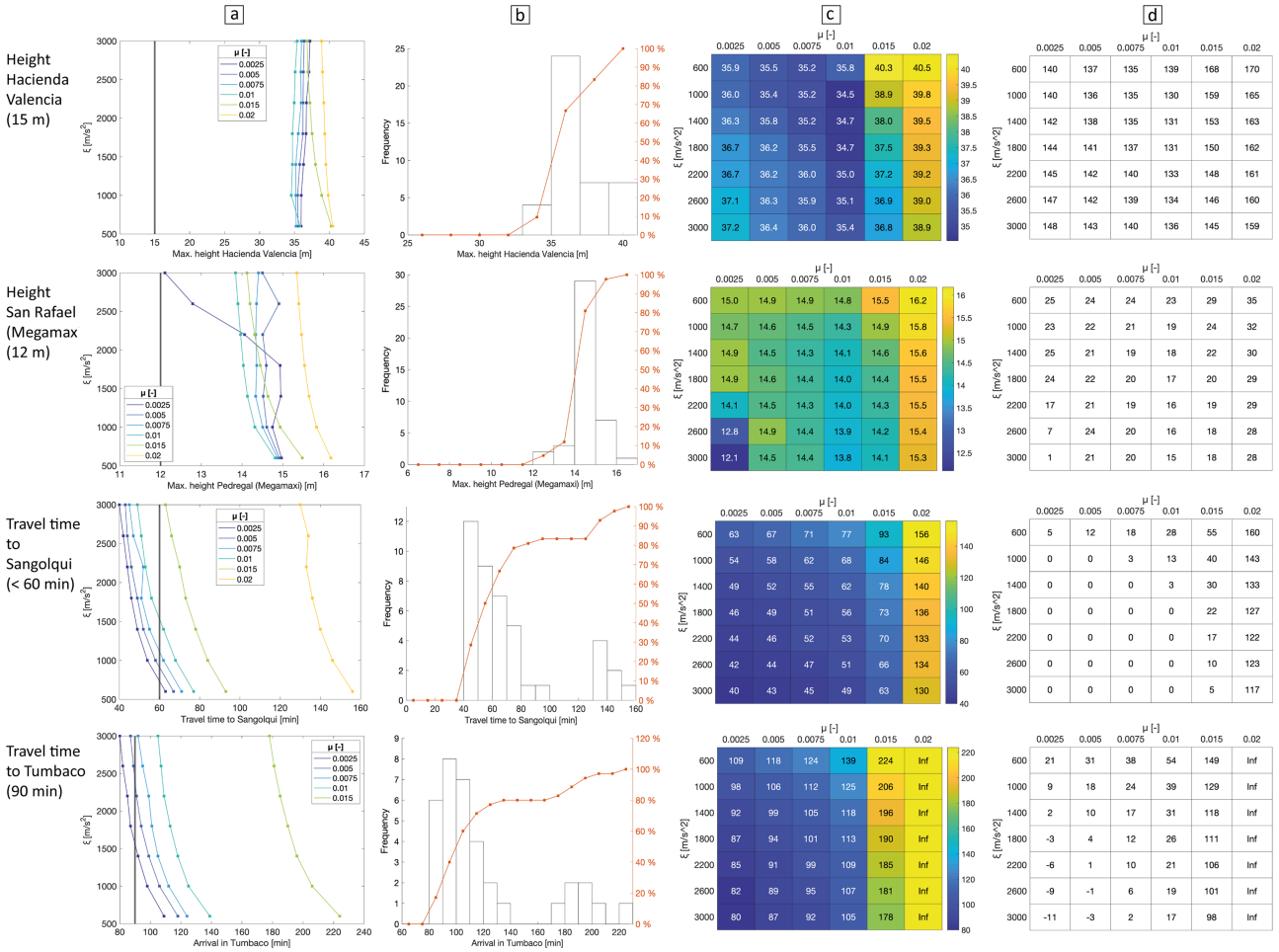

FIGURE 7 Model outcomes for calibration criteria for flow height and travel time. The target value of each criterion is given in brackets. (a) Sensitivity of the model outcome as a function of μ and ξ; (b) statistical analysis grouping frequency of model outcomes; (c) a visual, colour-coded matrix of model outcomes indicating increasing values of the considered measure from blue to yellow; (d) a visual matrix representing the performance of a simulation (ϕ) in terms of model deviation from target value. The calibration constraints of one measure type are displayed in order of their distance to the volcano [Colour figure can be viewed at wileyonlinelibrary.com]

large uncertainties in the target value itself. At San Rafael (Megamaxi), deviations are on the order of 25%, whereas at Hacienda Valencia, simulated flow heights exceed target values by 130–170%. As indicated in the frequency distribution (Figure 7, column b), the majority of model runs (60%) predict maximum flow heights at Hacienda Valencia between 35 and 37 m compared to the targeted value of 15 m. Using travel times as calibration constraints, we can observe a high sensitivity of this measure to μ, and a minor influence of ξ. The results further show that simulated travel times largely coincide with historical eyewitness reports. Simulation results for peak discharge measures react sensitively to variations in μ, but are largely insensitive to variations in ξ. We particularly note that the simulation of the overflow into the headwaters of the Rio Sta. Clara is a crucial constraint for the evaluation of model performance. We observe that all model runs reproduced a spillover at 'La Caldera', although approximately 90% of them underpredict the targeted maximum discharge. Interestingly, we can particularly well observe in animations of our model that flow bifurcation at La Caldera may not be a result of a real run-up of the flow front against the nearly vertical northern channel wall. The lahar is capable of passing the sharp curve at La Caldera, but as the downstream Pita canyon significantly narrows, the flow gets slowed down, leading to progressive upstream filling of the canyon until exceeding the height of the northern channel wall after about 90 s. The model results depicting simulated impact areas (maximum flow height > 0.05 m) correspond well with the mapped impact areas, with an overall good similarity among the model runs ranging between 79 and 86%.

As expected, the best-fitting μ/ξ combinations for each calibration measure with least deviations from target values are clustered at slightly different locations within the visual matrix (Figures 6, 7 and 8, column d). Without introducing subjective weighting for specific calibration criteria or types of calibration measures, we equally considered all criteria for deriving a final value of total model performance (Equation 10). Our analysis shows that model runs using $\mu = 0.005/\xi = 1400$ m/s^2 and $\mu = 0.0025/\xi = 1000$ m/s^2 produced the most representative overall simulations of the 1877 lahar, revealed by a performance value quantified as total model deviation of 23% for both combinations (Figure 8, red box). Importantly, the results demonstrate that the best-fit parameters fall into a broad zone of low deviation values.

The simulations of flow height, velocity and lahar erosion of a model run with $\mu = 0.005$ and $\xi = 1400$ m/s^2 are illustrated in Figure 5, and model performance for this best-fit parameter combination can be summarized from Figures 6, 7 and 8 as follows. (i) The

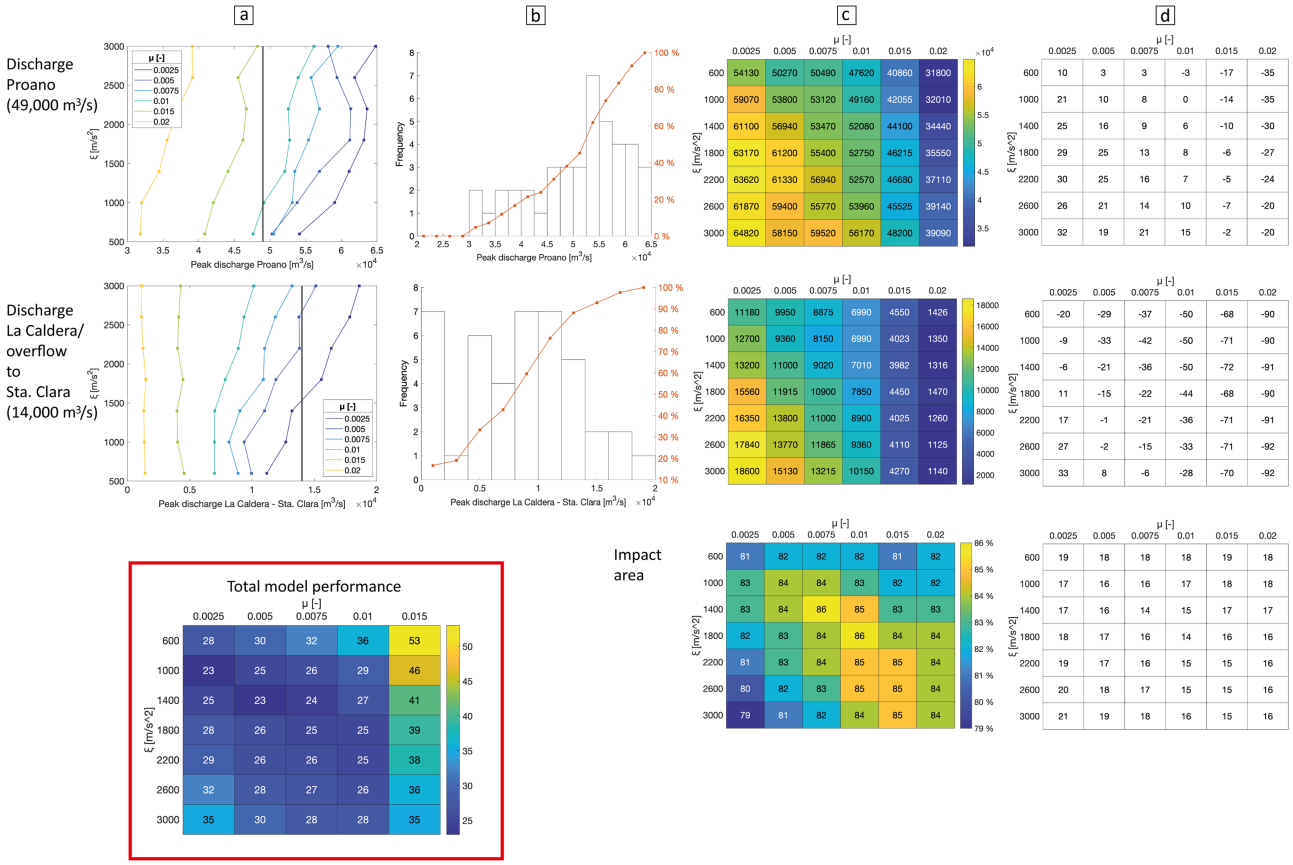

FIGURE 8 : Model outcomes for calibration criteria for peak discharge and impact area. The target value of each criterion is given in brackets. (a) Sensitivity of the model outcome as a function of μ and ξ; (b) statistical analysis grouping frequency of model outcomes; (c) a visual, colour-coded matrix of model outcomes indicating increasing values of the considered measure from blue to yellow; (c) a visual matrix representing the performance of a simulation (ϕ) in terms of model deviation from target value. The red box shows the simulation performance ϕ_{total} (quantified as percentage deviation) under consideration of all calibration criteria. μ/ξ combinations that best represent the 1877 lahar are indicated in dark blue [Colour figure can be viewed at wileyonlinelibrary.com]

impact area is well reproduced (model deviation of 16%) and traces the main flow paths, indicating that the model captures key features such as bifurcation and confluence of the flow. In the northern low-gradient area between the El Salto and Rio Pita streams, lateral spreading of the lahar is overestimated, which contributes to the observed model deviations. (ii) Flow velocities are very well reproduced with deviations of respectively 14, −1 and 3% at Jatabamba, Proano and Hacienda San Rafael. (iii) While simulated flow heights at Hacienda San Rafael and San Rafael (Megamaxi) show deviations from target values of 25 and 21%, flow heights at Hacienda Valencia are overestimated by 138%, possibly due to difficulties in delimiting flow limits in distal reaches. (iv) Travel times to Sangolquí and Tumbaco lie very well within the range of reported arrival times, deviating by 0 and 10%, respectively. (v) The peak discharge at Proano is slightly overestimated by the model, with a value of 10%. The overflow into the Sta. Clara River at La Caldera is reproduced with a deviation of −20%.

4.3 | Simulation of potential future lahars

We applied the calibrated lahar model with previously derived best-fitting input parameters (μ = 0.005 and ξ = 1400 m/s^2) and estimates of initial volume and discharge of the 1877 lahar to potential future lahars during three different eruption scenarios at Cotopaxi. Our approach to assess future lahar volumes considering the effect of glacier retreat yielded the following hydrograph estimates (Figure 9): for Scenarios 2, 3 and 4 in the northern drainage, we calculate peak discharges of respectively 32 000, 64 000 and 128 000 m^3/s and corresponding input volumes of 7.8, 18.9 and 46 × 10^6 m^3. In the southern drainage, we derive for Scenarios 2, 3 and 4 peak discharges of respectively 33 600, 67 300 and 134 500 m^3/s and corresponding input volumes of 8.3, 20.2 and 49 × 10^6 m^3.

The results of the scenario simulations are summarized in Table 2 and Figure 10; more detailed simulation results of flow heights, flow speed and erosion are provided in the online supporting information. We observed that simulated lahars in the northern drainage reach total flow volumes of ∼20 × 10^6 m^3 in Scenario 2, ∼35 × 10^6 m^3 in Scenario 3, and ∼70 × 10^6 m^3 in Scenario 4, which corresponds to a volume growth due to entrainment of 150, 80 and 50%, respectively. Potential lahars in all three eruption scenarios transit through the densely inhabited urban agglomeration of Valle de Los Chillos (including the town of San Rafael) via the Rio Pita, are then channelized in the Rio San Pedro and reach out to the city of Tumbaco and locations further downstream (outside the modelling region). Simulated travel times to San Rafael range between 84 min (Scenario 2) and 60 min (Scenario 4). An overflow at La Caldera and entering the Sta. Clara River occurs, to a minor degree, in Scenario 3, but only in Scenario

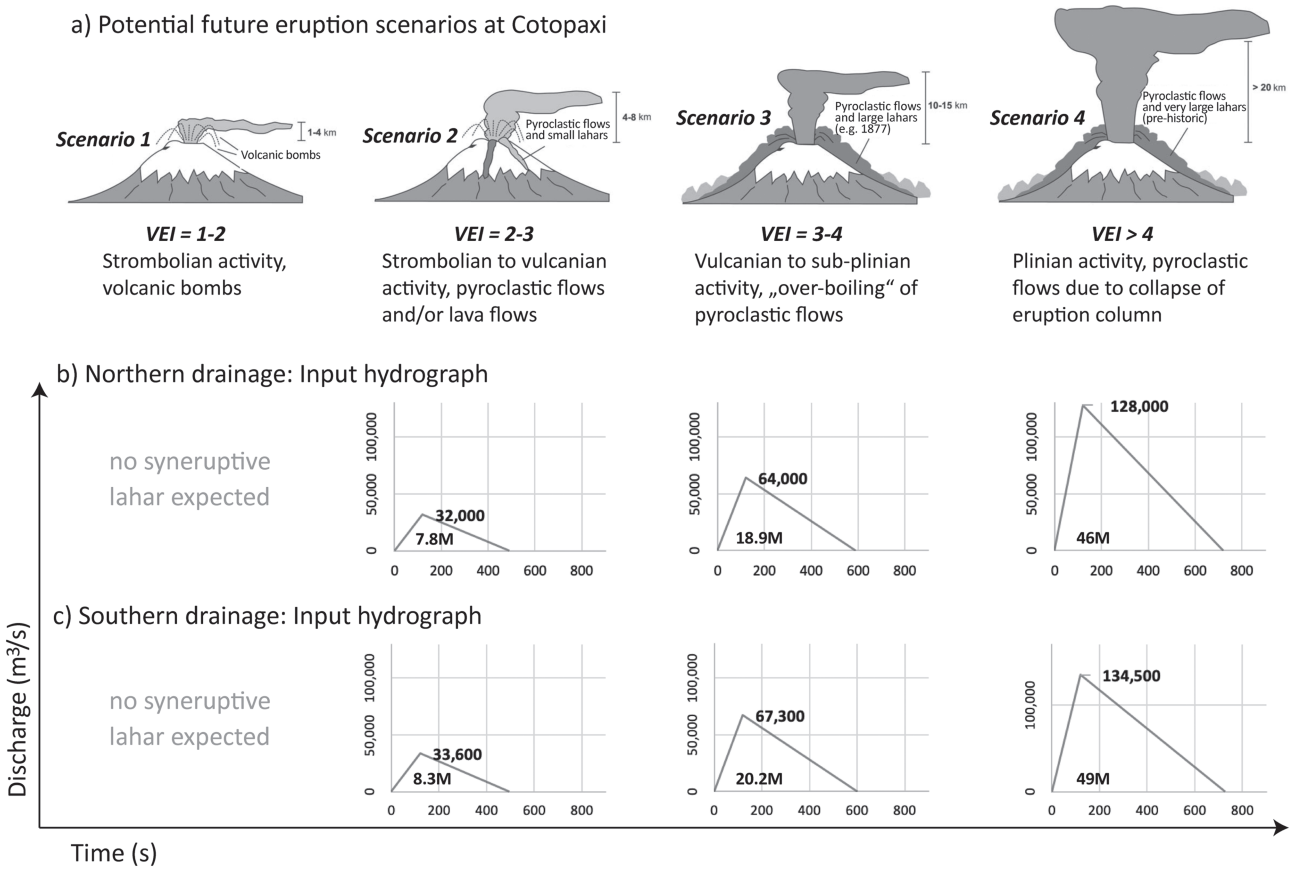

FIGURE 9 (a) Potential future eruption scenarios at Cotopaxi (Andrade et al., 2005), with corresponding input hydrographs for lahar modelling in the northern (b) and southern (c) drainage system

TABLE 2 Simulation results for potential future lahars in the northern and southern drainage of Cotopaxi (μ = 0.005/ξ = 1400 m/s^2) triggered by explosive eruptions with magnitudes of VEI 2–3, VEI 3–4 and VEI > 4. Comparison of simulated eroded volumes to input volumes yields a scenario- and drainage-specific volume growth. Simulated travel times are presented for selected settlements along the lahar runout paths

	Scenario 2 VEI 2–3	Scenario 3 VEI 3–4	Scenario 4 VEI > 4
Northern drainage			
Input flow volume [$\times 10^6$ m^3]	7.8	18.9	46
Eroded volume [$\times 10^6$ m^3]	11.6	15.7	24.7
Total flow volume [$\times 10^6$ m^3]/Volume growth	19.4/150%	34.6/80%	70.7/50%
Travel time to Sangolquí [min]	–	–	52
Travel time to San Rafael (Rio Pita) [min]	84	71	60
Southern drainage			
Input flow volume [$\times 10^6$ m^3]	8.3	20.2	49
Eroded volume [$\times 10^6$ m^3]	33.1	35.9	42.9
Total flow volume [$\times 10^6$ m^3]/Volume growth	41.4/400%	56.1/180%	91.9/90%
Travel time to Chasqui (Rio Cutuchi) [min]	18	17	15
Travel time to Mulaló (Rio Saquimala) [min]	18	18	17
Travel time to Lasso (Rio Cutuchi) [min]	32	30	26
Travel time to Latacunga [min]	60	58	54

4 is the overflow discharge large enough so that the lahar can propagate to the town of Sangolqui within 52 min and afterwards unite with the lahar in the Rio Pita channel.

Future lahars descending the southern channels reach total flow volumes of ~40 × 10^6 m^3 in Scenario 2, ~55 × 10^6 m^3 in Scenario 3, and ~90 × 10^6 m^3 in Scenario 4, because the lahar volumes increase respectively by 400, 180 and 90% due to sediment incorporation. Volume growth of the lahar, especially during VEI 2–3 and VEI 3–4 eruptions, is thus notably higher in the southern drainage. Lahars in all three scenarios reach the city of Salcedo and further downstream, but the inundation width in the densely populated Inter-Andean valley varies significantly in the section north of Latacunga, in

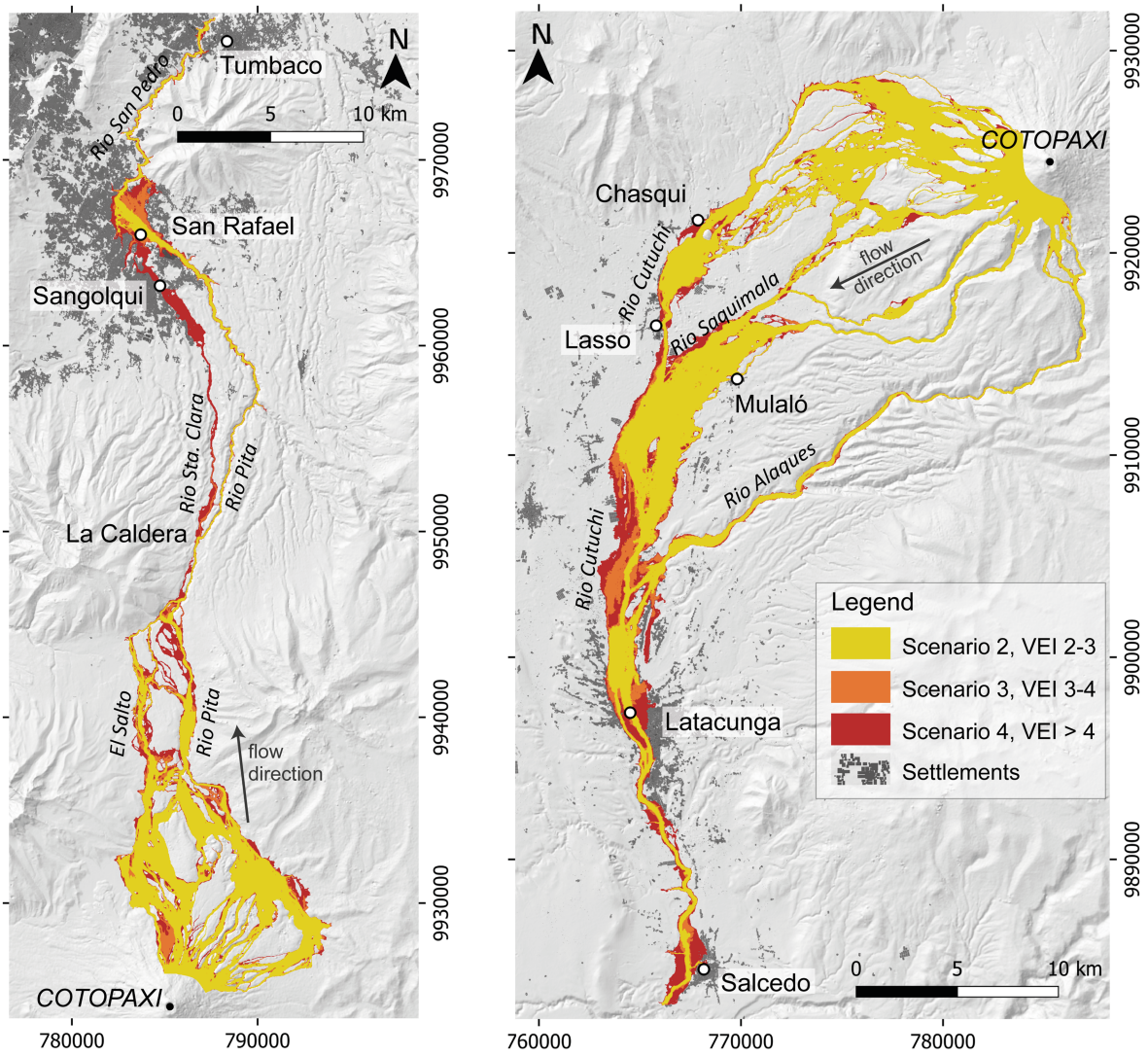

FIGURE 10 Lahar impact areas of potential lahars in the northern (a) and southern (b) drainage system generated during three different future eruption scenarios. The simulations are performed with anticipated total lahar volumes of ~20 Mm^3 (Scenario 2), ~35 Mm^3 (Scenario 3) and ~70 Mm^3 (Scenario 4) in the northern drainage, and ~40 Mm^3 (Scenario 2), ~55 Mm^3 (Scenario 3) and ~90 Mm^3 (Scenario 4) in the southern drainage. The downstream limits of the simulations are placed approximately 70 km downstream of the crater and do not represent deposit termini of the lahars. Maps showing simulated flow heights, flow speed and erosion are provided in the online supporting information [Colour figure can be viewed at wileyonlinelibrary.com]

Latacunga city and in Salcedo city. The simulated arrival times of the southern lahars are largely insensitive to release magnitude as they differ only little among the three eruption scenarios. Arrival times to towns and villages located close to the volcano, such as Mulaló and Chasqui, vary the least (only 1–2 min), indicating that the steep relief on the volcano edifice favours strong acceleration of lahars triggered by small VEI 2–3 as well as by large VEI > 4 eruptions (see online supporting information on flow speeds for comparison). Besides, the simulated transit times to Latacunga compare favourably with those reported by eyewitnesses of the 1877 event (<1 h).

5 | DISCUSSION

This study simulated an entire flow from Cotopaxi's upper volcano flank to distal impact areas using the 2-D software RAMMS debris flow for the first time. This implies investigating the applicability of a Voellmy–Salm rheology for lahar simulation purposes, which we achieved by model calibration and performance evaluation. A realistic parametrization of flow behaviour necessarily involves estimating the erosion capacity of lahars and analysing the influence of erosion and entrainment on flow volumes.

5.1 | Estimation of erosion capacity

To estimate erosion and entrainment by lahars, we used a forward modelling approach, which is based on estimating the erodibility of the substrate and is independent of the magnitude of an eruptive event. We demonstrated that lahars from Cotopaxi may experience substantial bulking during downstream propagation (for details, see Table 2).

Our simulations imply (Figure 11) that important volumetric additions to the flow almost entirely occur on the steep volcano slopes between 0 and ~20 min from event initiation. This reflects qualitatively the common understanding of how syneruptive lahars on ice-

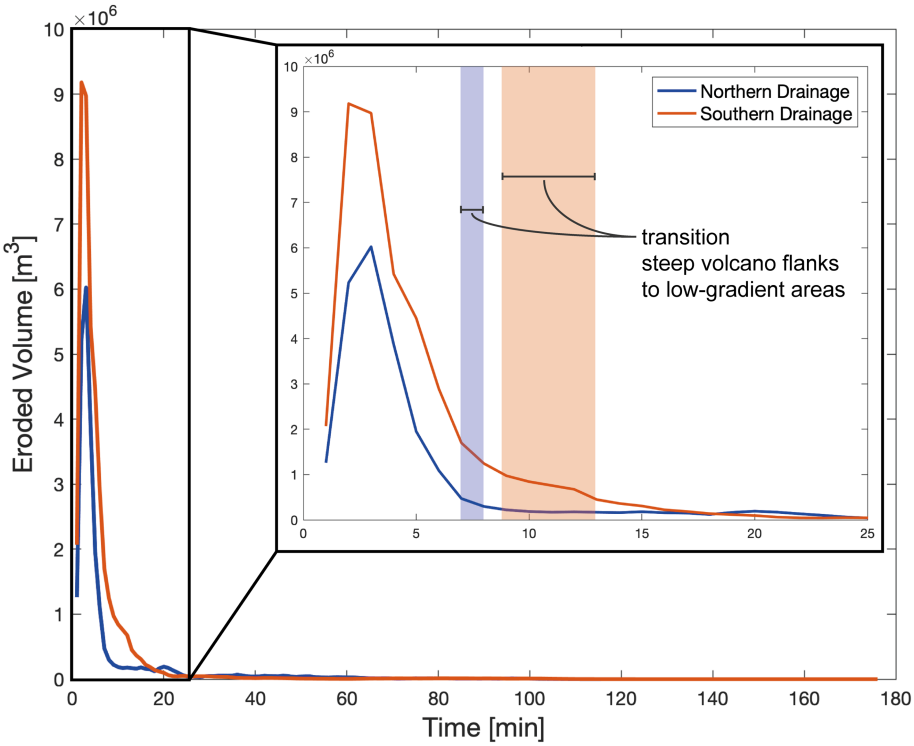

FIGURE 11 Eroded volume by lahars in the northern (blue) and southern (red) drainage as a function of simulation time (output in 60 s intervals). The northern and southern lahar started with an initial volume of 46×10^6 and 49×10^6 m^3, respectively, and simulations of both lahars are performed with $\mu = 0.005$ and $\xi = 1400$ m/s^2. The release hydrograph in the southern sector is placed higher on the volcano flank, increasing the distance over which the flow overruns loose and easily erodible volcaniclastic material [Colour figure can be viewed at wileyonlinelibrary.com]

clad volcanoes evolve: rapidly transitioning from an initially more dilute flow to a hyperconcentrated flow or debris flow due to coincident entrainment of pyroclastic material in proximal regions (Major & Newhall, 1989; Pierson et al., 1990). The reasons for the modelled spatial concentration of erosional impact at Cotopaxi's flanks are related to (i) the steep relief (Figure 1c), which results in large simulated shear stresses (Equation 5), and (ii) the prevalent loose and easily erodible pyroclastic material (Figure 2), which facilitates high erosion rates (Table 1). The impact of topography on modelled erosive forces is also evident in the significant reduction in eroded volume as the lahars enter low-gradient areas at the foot of the volcano (see Figure 11: after 7–8 and 9–13 min in the northern and southern drainage, respectively).

In contrast to previous models at Cotopaxi, this paper calculates erosivity along the entire initial steep and the flatter channelized trajectory, whereas previous models have only anticipated the latter. To compare erosion in low-gradient reaches, we estimate that a lahar of similar magnitude like in 1877 (Figure 11 and Table 2, Scenario 4) grows only by $\sim 4.5 \times 10^6$ m^3 (~6% of total volume) on entering the flatter northern trajectory, and by $\sim 6 \times 10^6$ m^3 (~6% of total volume) along the southern trajectory in the Inter-Andean Valley. Our numbers are very similar to calculated theoretical bulking values of previous lahar models at Cotopaxi: Aguilera et al. (2004) calculated for the northern 1877 lahar a theoretical, erosion-related growth of 3×10^6 m^3 (<5% of assumed total volume of 60×10^6 m^3), by relating flow height and channel slope to observed bulking values of Nevado del Ruíz lahars (Pierson et al., 1990). Using the same empirical relation, Pistolesi et al. (2014) found for the southern 1877 lahar a bulking value of 8.5×10^6 m^3 (7% of assumed total volume of 120×10^6 m^3).

In terms of quantifying total eroded volumes of future lahars from Cotopaxi, it was found that they may erode and entrain between $\sim 12 \times 10^6$ and $\sim 43 \times 10^6$ m^3 of substrate material, and can potentially grow in volume by 50–400% compared to initial volume over a modelled travel distance of ~70 km (Table 2). However, we cannot validate these values in absolute numbers because there are no quantitative erosion data available for lahars from Cotopaxi. Nevertheless, we can compare them to the 1985 Nevado del Ruíz lahars due to similar characteristics related to (i) the total flow volume ($\sim 90 \times 10^6$ m^3), (ii) the triggering mechanism (VEI = 3 eruption), which generated pyroclastic flows interacting with the glacier cap, and (iii) the runout distance (70–100 km from the source). Moreover, (iv) recent models for lahars from Cotopaxi (Mothes et al., 2004; Ordóñez et al., 2013; Vera et al., 2019) use a bulking factor of 3 as a rule of thumb throughout all modelled eruption scenarios, which is the mean of the bulking factors of 2 to 4 reported for Nevado del Ruíz lahars (Pierson et al., 1990). However, volumetric growth observed at the 1985 Nevado del Ruiz event may not be directly transferable to Cotopaxi lahars for two reasons. First, the site-specific topography around the two volcanoes, and thus the exerted basal shear pressures by the flow, are notably different: at Nevado del Ruíz, river channels maintain steep gradients on average 30% to distances of 20–50 km from the volcano; whereas at Cotopaxi, slope gradients of this order only extend 4–8 km from the crater and drop after to about 1–10%. Steep channel gradients and the presence of erodible material downstream of Nevado del Ruíz favoured a large volume growth from initially 20×10^6 m^3 to about 70×10^6 m^3 due to sediment entrainment during downstream propagation (Pierson et al., 1990). This is about twice as much eroded sediment compared to our simulations at Cotopaxi, where a lahar with an initial volume of $\sim 20 \times 10^6$ m^3 (Scenario 3, southern drainage) may erode and entrain $\sim 36 \times 10^6$ m^3. Second, we found that volumetric growth of lahars may vary remarkably among the different future eruption scenarios: in the southern drainage, initial volumes of small lahars (Scenario 2) increase by ~400%, whereas lahars with large initial volumes (Scenario 4) grow by ~100%. This indicates that even small initial lahars from Cotopaxi are possibly capable of entraining large volumes of sediment, favoured by the presence of easily

erodible pyroclastic sediment on the volcano flanks with high erosion rates and low yield stresses (Table 1). The variations in volume growth have important implications for the estimation of future lahar magnitudes. Our simulations suggest that application of a volume growth factor of 3 may result in underestimation of bulk volumes of initially smaller-magnitude (VEI 2–3) lahars from Cotopaxi.

Spatial classification of the substrate into erodibility classes was carried out remotely for the most part, supported by field evidence at selective locations. This yielded reasonable ballpark estimates of amounts and spatial occurrence of lahar entrainment, but detailed field-based mapping of substrate types can further improve the predictive power. Nevertheless, it remains open whether the model parameters for erosion rates, potential erosion depths and yield stress assigned to each erodibility class (Table 1) can be used to infer erosion and entrainment by large-magnitude lahars, as these erosion parameters were derived from natural debris flows in the Alps (Frank et al., 2015). The loose, pyroclastic material present on the volcano flanks, which largely controls the volumetric growth of the lahar, was characterized by erosion rates twice as high as the average observed rates in the Illgraben catchment (Frank et al., 2017), but possibly the entrainment is even more extreme. Application to lahar events with documented spatial erosion patterns is needed to quantify possible deviations. We also note that the model is limited to predict material entrainment from vertical erosion in the channel bed, but does not consider additional volume sources such as channel bank collapse, (re-) activated major landslides along the channels and in source areas on the volcano, or freshly ejected volcaniclastic material, which may attain a thickness in proximal (<10 km) zones of 1–1.5 m during a future VEI > 4 eruption (Andrade et al., 2005).

5.2 | Model performance for lahar simulation

We back-calculated the 1877 lahar event at Cotopaxi and performed a multi-criteria calibration using calibration measures such as impact area, flow height, flow velocity, travel times and peak discharge (Mothes et al., 2004; Sodiro, 1877; Wolf, 1878). By evaluating model outcomes of all calibration constraints simultaneously, we could derive an overall good level of fit, not only for a single, but for a broader zone of frictional input parameter combinations, where model deviations are always smaller than 25% (Figure 8). This corroborates the robustness of the model and further suggests that the bulk behaviour of lahars can be adequately reproduced with the tested Voellmy–Salm rheology.

The calibration process is affected by uncertainties in reported total volume of the northern 1877 lahar (60×10^6 to 75×10^6 m^3), in our strategy to estimate the input hydrograph, and in the accuracy of the used DEM with regard to morphological change since 1877. Likewise, evaluation of model performance is largely based on comparing target values of calibration criteria to model outcomes. However, there is some uncertainty in the target values themselves, arising from error sources in super-elevation measurements to estimate peak flow velocity (Pierson & Scott, 1985; Prochaska et al., 2008), and from the degree of preservation of lahar deposits to estimate inundation limits and stage heights. The total model performance number is especially influenced by one outlier, the height constraint at Hacienda Valencia, where simulated values deviate strongly from targeted by 130–170%. At this location, simulated flow heights throughout the entire μ/ξ parameter space all have values between ~35 and 41 m, indicating that the simulation results seem statistically sound (Figure 7). The source of this deviation could have its origin in (i) the complicated determination of deposit termini and (ii) higher deviations in the DEM from pre-event channel topography with increasing distance from the volcano, which results from anthropogenic modifications and extensive vegetation growth in climatically favoured downstream valleys. Importantly, deviations in flow height can also be ascribed to the fact that (iii) target heights are estimated from final flow deposits while the model calculates maximum stage heights. These uncertainties in height estimates likely also apply to the results at San Rafael (Megamaxi). For such cases, the calibration approach developed by Aaron et al. (2019) would allow including a specific uncertainty for each criterion, but these have not been quantified in Mothes et al. (2004) and later estimation seems inappropriate. If we exclude the height constraint at Hacienda Valencia, the total performance value would lower to 13% compared to currently 23% for μ = 0.005/ξ = 1400 m/s^2.

We generally found that extremely low values for Coulomb-type friction μ and relatively high values for turbulent friction ξ best reproduce the behaviour of massive syneruptive lahars at Cotopaxi, and that μ has a stronger influence on model outcomes than ξ (Figures 6, 7 and 8). As this is the first application to syneruptive lahars, no back-analysed Voellmy parameters are currently available for comparison, and model application to other case studies is needed for further interpretation. The calibrated μ values (0.0025 and 0.005) are at least one order of magnitude smaller than those used for modelling non-volcanic debris flows (Hussin et al., 2012; Schraml et al., 2015), GLOFs (Frey et al., 2018; Schneider et al., 2014) or ice-rock avalanches (Schneider et al., 2010; Sosio et al., 2008). However, Sosio et al. (2011) used similar μ/ξ combinations (μ between 0.001 and 0.02, ξ between 700 and 1200 m/s^2) to simulate volcanic debris avalanches evolving from sudden failure of volcano flanks. An undisputable reason for our calibration result is that only small μ/large ξ combinations can reproduce the extremely long runout distances of lahars from Cotopaxi. A small value of μ and a larger value of ξ indicate low flow resistance (Equation (4)) and lead to a slow stopping mechanism, which in turn is the reason why the model fails to reproduce material deposition in the plains around the volcano. Large values of ξ further indicate that the turbulent friction term in Equation (4) is marginally relevant for the simulation of syneruptive lahars in this study.

5.3 | Simulation of future Cotopaxi lahars

Predicting the magnitude of future syneruptive lahars is an inherently difficult challenge, because it involves estimating the efficacy of volcano-glacier interactions during an eruption and consequent water supply, as well as the potential of material incorporation and volume growth of the lahar (Pierson, 1995). To anticipate the latter, we proposed a generic model approach and start the lahar on the steep upper volcano slopes in order to provide a first estimate of erosion capacity of lahars. As discussed previously, the scenario simulations revealed a variable degree of volume growth among the three potential future scenarios and the two drainages. This model approach can,

therefore, support the estimate of volcano-specific bulking factors of lahars.

In our model, the efficacy of volcano-glacier interactions is quantified in the release hydrograph of each eruption scenario, defining the volume of slurry produced by rapid mixing of hot eruption products with ice and snow. Similar to previous lahar studies at Cotopaxi (Aguilera et al., 2004; Barberi et al., 1992; Mothes et al., 2004), our estimations of initial volumes of future lahars are directly related to the glacier extent. Because the extent of Cotopaxi's glaciers has diminished by at least ~50% since the last major eruption in 1877 (Cáceres, 2017), we assumed that this would convert into a 50% reduction in initial volumes of future lahars. However, the degree to which glacier retreat influences resulting lahar volumes is an open issue. Pistolesi et al. (2013, 2014) argued that lahar magnitudes expected at Cotopaxi strongly depend on eruption dynamics and the type of lahar triggering mechanism: 1877-type eruptions (VEI 3–4) with boiling-over activity mostly produce scoria flows that erode deep, linear canyons into the glacier. Glacier extent could therefore have only a minor effect on initial lahar volumes. Consequently, future eruptions will presumably generate lahars similar in magnitude to that of 1877, despite a 50% reduction in glacier surface area. In contrast, VEI > 4 eruptions produce pyroclastic surges or flows that interact with the entire glacier cap, and glacier retreat would thus exert a major control on initial lahar volumes. In a nutshell, our study shows that Voellmy–Salm models can effectively and robustly anticipate future lahars, but it remains essential to communicate uncertainties involved in estimating future lahar magnitudes and consequently simulated lahar impact areas to decision-making authorities and downstream communities.

6 | CONCLUSION

In this study, we simulated massive long-distance lahars from Cotopaxi volcano, from initiation on the steep upper volcano flanks to distal reaches about 70 km from the source. The generic lahar model in RAMMS debris flow was back-calculated based on records of the destructive 1877 event (60–75 $\times$ 10^6 m^3 northern drainage, 80–100 $\times$ 10^6 m^3 southern drainage) and estimations on erosion capacity. The calibrated model was then applied to potential future lahars controlled by VEI-based eruption scenarios for Cotopaxi volcano. The key findings can be summarized as follows.

The tested Voellmy–Salm rheology plausibly and robustly reproduces key flow characteristics of massive syneruptive lahars. This is supported by an objective evaluation of model performance based on 14 calibration constraints of physical flow properties of the 1877 lahar, such as flow height, flow speed, peak discharge, travel time and impact area. The model results match especially well with observed impact area (deviation of 16%), flow velocities (deviations of −1 to 14%), travel times (deviations of 0 and 10%) and peak discharges (deviations of −20 to 10%), while simulated stage heights show larger deviations from target values. Due to the long runout of the lahar, extremely low values of Coulomb-type friction μ (0.0025–0.005) and high values of turbulent friction ξ (1000–1400 m/s^2) best reproduce the propagation of syneruptive lahars.

Lahar erosion is estimated by a forward model approach, that relies on the erodibility of the underlying substrate given by the current geological and topographical setting. The simulations demonstrate that the degree of volume growth decreases with release volume, ranging between 50% for large (46 $\times$ 10^6 m^3) and 400% for comparably smaller (8 $\times$ 10^6 m^3) initial volumes, respectively. Despite the uncertainties involved in this approach, the qualitative prediction of simulated lahar erosivity on the steep volcano flanks using the proposed straightforward estimation of erosion capacity is promising compared with observed spatial erosion patterns. Further information will be gained by transferring this approach to more recent lahar events, where quantitative and detailed spatial information about erosion by flow is readily available.

A reliable estimation of the magnitudes of future eruption-triggered lahars and according hazards to downstream communities is challenging and needs to consider the degree of volcano-glacier interactions as well as the degree of solids incorporation into the flow. The generic model approach developed in this study includes lahar erosivity and can help to anticipate the volumetric growth and runout patterns of syneruptive lahars. However, critical processes determining initial lahar magnitudes (i.e. eruption magnitude, eruption dynamics, interactions between volcanic products and ice/snow, impact of glacier retreat) are not thoroughly understood and need more dedicated research.

ACKNOWLEDGEMENTS

This study has been conducted as part of the project RIESGOS (Grant No. 03G0876D), funded by the German Federal Ministry of Education and Research (BMBF). The project involves the analysis of multi-risk situations and related cascading effects in selected pilot regions in Chile, Ecuador and Peru. In this context, we especially acknowledge the collaboration with IG-EPN Ecuador and also thank Franziska Petry and Andreas Dietrich for various discussions and input. The authors thank Marc Christen (SLF) and Brian McArdell (WSL) for discussions and support of the RAMMS model.

Open access funding enabled and organized by Projekt DEAL.

CONFLICT OF INTEREST

The authors declare that they have no conflict of interest.

DATA AVAILABILITY STATEMENT

The data that support the findings of this study are available from the corresponding author upon reasonable request.

ORCID

Theresa Frimberger https://orcid.org/0000-0002-0248-7292
S. Daniel Andrade https://orcid.org/0000-0002-4814-8691
Samuel Weber https://orcid.org/0000-0003-0720-5378
Michael Krautblatter https://orcid.org/0000-0002-2775-2742

REFERENCES

Aaron, J., McDougall, S. & Nolde, N. (2019) Two methodologies to calibrate landslide runout models. *Landslides*, 16(5), 907–920. https://doi.org/10.1007/s10346-018-1116-8

Aguilera, E., Pareschi, M., Rosi, M. & Zanchetta, G. (2004) Risk from lahars in the northern valleys of Cotopaxi Volcano (Ecuador). *Natural Hazards*, 33(2), 161–189. https://doi.org/10.1023/B:NHAZ.0000037037.03155.23

Andrade, D., Hall, M., Mothes, P., Troncoso, L., Eissen, J.-P., Samaniego, P. *et al.* (2005) *Los peligros volcánicos asociados con el Cotopaxi*. Corporación Editora Nacional, CEN/Escuela Politécnica Nacional: Quito.

Auker, M.R., Sparks, R.S.J., Siebert, L., Crosweller, H.S. & Ewert, J. (2013) A statistical analysis of the global historical volcanic fatalities record. *Journal of Applied Volcanology*, 2, art. 2. https://doi.org/10.1186/2191-5040-2-2

Barberi, F., Caruso, P., Macedonio, G., Pareschi, M. & Rosi, M. (1992) Reconstruction and numerical simulation of the lahar of the 1877 eruption of Cotopaxi volcano (Ecuador). *Acta Vulcanologica*, 2, 35–44.

Barberi, F., Coltelli, M., Frullani, A., Rosi, M. & Almeida, E. (1995) Chronology and dispersal characteristics of recently (last 5000 years) erupted tephra of Cotopaxi (Ecuador): Implications for long-term eruptive forecasting. *Journal of Volcanology and Geothermal Research*, 69(3–4), 217–239. https://doi.org/10.1016/0377-0273(95)00017-8

Bartelt, P., Bieler, C., Buehler, Y., Christen, M., Deubelbeiss, Y., Graf, C., *et al.* (2017) *RAMMS::DEBRISFLOW User Manual*. ETH: Zürich.

Bartelt, P., Salm, B. & Gruber, U. (1999) Calculating dense-snow avalanche runout using a Voellmy-fluid model with active/passive longitudinal straining. *Journal of Glaciology*, 45(150), 242–254. https://doi.org/10.1017/S002214300000174X

Berger, C., McArdell, B.W., Fritschi, B. & Schlunegger, F. (2010) A novel method for measuring the timing of bed erosion during debris flows and floods. *Water Resources Research*, 46, W02502. https://doi.org/10.1029/2009WR007993

Berger, C., McArdell, B.W. & Schlunegger, F. (2011) Sediment transfer patterns at the Illgraben catchment, Switzerland: Implications for the time scales of debris flow activities. *Geomorphology*, 125(3), 421–432. https://doi.org/10.1016/j.geomorph.2010.10.019

Bernard, B., Battaglia, J., Proaño, A., Hidalgo, S., Vásconez, F., Hernandez, S. & Ruiz, M. (2016) Relationship between volcanic ash fallouts and seismic tremor: Quantitative assessment of the 2015 eruptive period at Cotopaxi volcano, Ecuador. *Bulletin of Volcanology*, 78(11), 80. https://doi.org/10.1007/s00445-016-1077-5

Berti, M., Genevois, R., Simoni, A. & Tecca, P.R. (1999). Field observations of a debris flow event in the Dolomites. *Geomorphology*, 29(3–4), 265–274. https://doi.org/10.1016/S0169-555X(99)00018-5

Beverage, J.P. & Culbertson, J.K. (1964). Hyperconcentrations of suspended sediment. *Journal of the Hydraulics Division, ASCE*, 90, 117–128.

Brown, S.K., Jenkins, S.F., Sparks, R.S.J., Odbert, H. & Auker, M.R. (2017) Volcanic fatalities database: Analysis of volcanic threat with distance and victim classification. *Journal of Applied Volcanology*, 6, 1–20.

Caballero, L. & Capra, L. (2014) The use of FLO2D numerical code in lahar hazard evaluation at Popocatépetl volcano: A 2001 lahar scenario. *Natural Hazards and Earth System Sciences*, 14(12), 3345–3355. https://doi.org/10.5194/nhess-14-3345-2014

Cáceres, B. (2017) The role of geosciences in societal development: A German–Latin American perspective. In *Evolución de los glaciares del Ecuador durante los últimos 60 años y su relación con el cambio climático*, p. 149.

Carrivick, J.L. (2007) Modelling coupled hydraulics and sediment transport of a high-magnitude flood and associated landscape change. *Annals of Glaciology*, 45, 143–154. https://doi.org/10.3189/172756407782282480

Carrivick, J.L., Manville, V. & Cronin, S.J. (2008) A fluid dynamics approach to modelling the 18th March 2007 lahar at Mt. Ruapehu, New Zealand. *Bulletin of Volcanology*, 71, 153–169.

Carrivick, J.L., Manville, V., Graettinger, A. & Cronin, S.J. (2010) Coupled fluid dynamics–sediment transport modelling of a crater lake breakout lahar: Mt. Ruapehu, New Zealand. *Journal of Hydrology*, 388(3–4), 399–413. https://doi.org/10.1016/j.jhydrol.2010.05.023

Christen, M., Kowalski, J. & Bartelt, P. (2010) RAMMS: Numerical simulation of dense snow avalanches in three-dimensional terrain. *Cold Regions Science and Technology*, 63(1–2), 1–14. https://doi.org/10.1016/j.coldregions.2010.04.005

Costa, J.E. (1984) *Physical Geomorphology of Debris Flows. Developments and Applications of Geomorphology*. Springer: Berlin.

Delaite, G., Thouret, J., Sheridan, M., Labazuy, P., Stinton, A., Souriot, T. & van Westen, C. (2005) Assessment of volcanic hazards of El Misti and in the city of Arequipa, Peru, based on GIS and simulations, with emphasis on lahars. *Zeitschrift für Geomorphologie*, 140, 209–231.

Dietrich, A. & Krautblatter, M. (2019) Deciphering controls for debris-flow erosion derived from a LiDAR-recorded extreme event and a calibrated numerical model (Roßbichelbach, Germany). *Earth Surface Processes and Landforms*, 44(6), 1346–1361. https://doi.org/10.1002/esp.4578

Doyle, E., Cronin, S. & Thouret, J.-C. (2011) Defining conditions for bulking and debulking in lahars. *Bulletin*, 123, 1234–1246.

Fagents, S.A. & Baloga, S.M. (2006) Toward a model for the bulking and debulking of lahars. *Journal of Geophysical Research*, 111, B10201. https://doi.org/10.1029/2005JB003986

Fischer, J.-T., Kowalski, J. & Pudasaini, S.P. (2012) Topographic curvature effects in applied avalanche modeling. *Cold Regions Science and Technology*, 74, 21–30.

Frank, F., McArdell, B.W., Huggel, C. & Vieli, A. (2015) The importance of entrainment and bulking on debris flow runout modeling: Examples from the Swiss Alps. *Natural Hazards and Earth System Sciences*, 15 (11), 2569–2583. https://doi.org/10.5194/nhess-15-2569-2015

Frank, F., McArdell, B.W., Oggier, N., Baer, P., Christen, M. & Vieli, A. (2017) Debris-flow modeling at Meretschibach and Bondasca catchments, Switzerland: Sensitivity testing of field-data-based entrainment model. *Natural Hazards and Earth System Sciences*, 17(5), 801–815. https://doi.org/10.5194/nhess-17-801-2017

Frey, H., Huggel, C., Chisolm, R.E., Baer, P., McArdell, B., Cochachin, A. & Portocarrero, C. (2018) Multi-source glacial lake outburst flood hazard assessment and mapping for Huaraz, Cordillera Blanca, Peru. *Frontiers in Earth Science*, 6. https://doi.org/10.3389/feart.2018.00210

Gaunt, H.E., Bernard, B., Hidalgo, S., Proaño, A., Wright, H., Mothes, P. *et al.* (2016) Juvenile magma recognition and eruptive dynamics inferred from the analysis of ash time series: The 2015 reawakening of Cotopaxi volcano. *Journal of Volcanology and Geothermal Research* 328, 134–146. https://doi.org/10.1016/j.jvolgeores.2016.10.013

Hall, M. & Mothes, P. (2008) The rhyolitic–andesitic eruptive history of Cotopaxi volcano, Ecuador. *Bulletin of Volcanology*, 70(6), 675–702. https://doi.org/10.1007/s00445-007-0161-2

Hidalgo, S., Battaglia, J., Arellano, S., Sierra, D., Bernard, B., Parra, R. *et al.* (2018) Evolution of the 2015 Cotopaxi eruption revealed by combined geochemical and seismic observations. *Geochemistry, Geophysics, Geosystems*, 19(7), 2087–2108. https://doi.org/10.1029/2018GC007514

Huggel, C., Schneider, D., Miranda, P.J., Delgado Granados, H. & Kääb, A. (2008) Evaluation of ASTER and SRTM DEM data for lahar modeling: A case study on lahars from Popocatépetl volcano, Mexico. *Journal of Volcanology and Geothermal Research*, 170(1–2), 99–110. https://doi.org/10.1016/j.jvolgeores.2007.09.005

Hungr, O. & McDougall, S. (2009) Two numerical models for landslide dynamic analysis. *Computers & Geosciences*, 35(5), 978–992. https://doi.org/10.1016/j.cageo.2007.12.003

Hussin, H.Y., Quan Luna, B., van Westen, C.J., Christen, M., Malet, J.P. & van Asch, T.W.J. (2012) Parameterization of a numerical 2-D debris flow model with entrainment: A case study of the Faucon catchment, Southern French Alps. *Natural Hazards and Earth System Sciences*, 12 (10), 3075–3090. https://doi.org/10.5194/nhess-12-3075-2012

Iverson, R.M. (1997) The physics of debris flows. *Reviews of Geophysics*, 35 (3), 245–296. https://doi.org/10.1029/97RG00426

Iverson, R.M. (2012) Elementary theory of bed-sediment entrainment by debris flows and avalanches. *Journal of Geophysical Research - Earth Surface*, 117. https://doi.org/10.1029/2011JF002189

Iverson, R.M. & Denlinger, R.P. (2001) Flow of variably fluidized granular masses across three-dimensional terrain: 1. Coulomb mixture theory. *Journal of Geophysical Research - Solid Earth*, 106(B1), 537–552. https://doi.org/10.1029/2000JB900329

Iverson, R.M. & George, D.L. (2016) Modelling landslide liquefaction, mobility bifurcation and the dynamics of the 2014 Oso disaster. *Géotechnique*, 66(3), 175–187. https://doi.org/10.1680/jgeot.15.LM.004

Iverson, R.M., Logan, M., LaHusen, R.G. & Berti, M. (2010) The perfect debris flow? Aggregated results from 28 large-scale experiments. *Journal of Geophysical Research - Earth Surface*, 115. https://doi.org/10.1029/2009JF001514

Iverson, R.M. & Ouyang, C. (2015) Entrainment of bed material by earth-surface mass flows: Review and reformulation of depth-integrated theory. *Reviews of Geophysics*, 53(1), 27–58. https://doi.org/10.1002/2013RG000447

Iverson, R.M., Reid, M.E., Logan, M., LaHusen, R.G., Godt, J.W. & Griswold, J.P. (2011) Positive feedback and momentum growth during debris-flow entrainment of wet bed sediment. *Nature Geoscience*, 4(2), 116–121. https://doi.org/10.1038/ngeo1040

Iverson, R.M., Schilling, S.P. & Vallance, J.W. (1998) Objective delineation of lahar-inundation hazard zones. *Geological Society of America Bulletin*, 110(8), 972–984. https://doi.org/10.1130/0016-7606(1998)110<0972:ODOLIH>2.3.CO;2

Lee, S.-K., Lee, C.-W. & Lee, S. (2015) A comparison of the Landsat image and LAHARZ-simulated lahar inundation hazard zone by the 2010 Merapi eruption. *Bulletin of Volcanology*, 77(6), 46. https://doi.org/10.1007/s00445-015-0920-4

Lube, G., Cronin, S.J. & Procter, J.N. (2009) Explaining the extreme mobility of volcanic ice-slurry flows, Ruapehu volcano, New Zealand. *Geology*, 37(1), 15–18. https://doi.org/10.1130/G25352A.1

Lupiano, V., Chidichimo, F., Machado, G., Catelan, P., Molina, L., Calidonna, C.R. *et al.* (2020) From examination of natural events to a proposal for risk mitigation of lahars by a cellular-automata methodology: A case study for Vascún valley, Ecuador. *Natural Hazards and Earth System Sciences*, 20(1), 1–20. https://doi.org/10.5194/nhess-20-1-2020

Lupiano, V., Machado, G. & Di Gregorio, S. (2018) Revisiting the 1877 cataclysmic lahars of Cotopaxi volcano by a cellular automata model and implications for future events. In *Proceedings of the 2nd International Conference on Computer Science and Application Engineering*, pp. 1–7.

Machado, G., Lupiano, V., Avolio, M.V., Gullace, F. & Di Gregorio, S. (2015) A cellular model for secondary lahars and simulation of cases in the Vascún Valley, Ecuador. *Journal of Computational Science*, 11, 289–299. https://doi.org/10.1016/j.jocs.2015.08.001

Major, J.J. & Newhall, C.G. (1989) Snow and ice perturbation during historical volcanic eruptions and the formation of lahars and floods. *Bulletin of Volcanology*, 52(1), 1–27. https://doi.org/10.1007/BF00641384

Mangeney, A. (2011) Landslide boost from entrainment. *Nature Geoscience*, 4(2), 77–78. https://doi.org/10.1038/ngeo1077

Manville, V. (2004) Palaeohydraulic analysis of the 1953 Tangiwai lahar; New Zealand's worst volcanic disaster. *Acta Vulcanologica*, 16(1–2), 137–152.

McArdell, B.W., Bartelt, P. & Kowalski, J. (2007) Field observations of basal forces and fluid pore pressure in a debris flow. *Geophysical Research Letters*, 34(7). https://doi.org/10.1029/2006GL029183

McCoy, S.W., Kean, J.W., Coe, J.A., Tucker, G.E., Staley, D.M. & Wasklewicz, T.A. (2012) Sediment entrainment by debris flows: In situ measurements from the headwaters of a steep catchment. *Journal of Geophysical Research - Earth Surface*, 117, F03016. https://doi.org/10.1029/2011JF002278

McDougall, S. (2006) *A new continuum dynamic model for the analysis of extremely rapid landslide motion across complex 3D terrain*. PhD thesis, University of British Columbia.

McDougall, S. & Hungr, O. (2005) Dynamic modelling of entrainment in rapid landslides. *Canadian Geotechnical Journal*, 42(5), 1437–1448. https://doi.org/10.1139/t05-064

Mizuyama, T., Kobashi, S. & Ou, G. (1992) Prediction of debris flow peak discharge. *Internationales symposion: Interpraevent*: 99–108.

Mothes, P., Espin, P., Hall, M., Vasconez, F., Sierra, D. & Andrade, D. (2016) *Mapa regional de amenazas volcánicas potenciales del volcán Cotopaxi, zona norte*. Instituto Geofísico de la Escuela Politécnica Nacional.

Mothes, P., Hall, M.L., Andrade, D., Yepes, H., Pierson, T.C., Gorki Ruiz, A. & Samaniego, P. (2004) Character, stratigraphy and magnitude of historical lahars of Cotopaxi volcano (Ecuador). *Acta Vulcanologica*, 16(1–2), 85–108.

Mothes, P.A., Hall, M.L. & Janda, R.J. (1998) The enormous Chillos Valley Lahar: An ash-flow-generated debris flow from Cotopaxi Volcano, Ecuador. *Bulletin of Volcanology*, 59(4), 233–244. https://doi.org/10.1007/s004450050188

Mothes, P.A., Ruiz, M.C., Viracucha, E.G., Ramón, P.A., Hernández, S., Hidalgo, S. *et al.* (2017) Geophysical footprints of Cotopaxi's unrest and minor eruptions in 2015: An opportunity to test scientific and community preparedness. In , Unrest, V., Gottsmann, J., Neuberg, J., Scheu, B. (eds). Springer: Cham; 241–270.

Muñoz-Salinas, E., Castillo-Rodríguez, M., Manea, V., Manea, M. & Palacios, D. (2009) Lahar flow simulations using LAHARZ program: Application for the Popocatépetl volcano, Mexico. *Journal of Volcanology and Geothermal Research*, 182(1–2), 13–22. https://doi.org/10.1016/j.jvolgeores.2009.01.030

Newhall, C.G. & Self, S. (1982) The volcanic explosivity index (VEI) an estimate of explosive magnitude for historical volcanism. *Journal of Geophysical Research, Oceans*, 87(C2), 1231–1238. https://doi.org/10.1029/JC087iC02p01231

O'Brien, J.S., Julien, P.Y. & Fullerton, W. (1993) Two-dimensional water flood and mudflow simulation. *Journal of Hydraulic Engineering*, 119(2), 244–261. https://doi.org/10.1061/(ASCE)0733-9429(1993)119:2(244)

Ordóñez, J., Samaniego, P., Mothes, P. & Schilling, S. (2013) *Las potenciales zonas de inundación por lahares en el volcán Cotopaxi*. Publicación Instituto Geofísico-Escuela Politécnica Nacional, N. 20.

Pierson, T.C. (1995) Flow characteristics of large eruption-triggered debris flows at snow-clad volcanoes: Constraints for debris-flow models. *Journal of Volcanology and Geothermal Research*, 66(1–4), 283–294. https://doi.org/10.1016/0377-0273(94)00070-W

Pierson, T.C. (1998) An empirical method for estimating travel times for wet volcanic mass flows. *Bulletin of Volcanology*, 60(2), 98–109. https://doi.org/10.1007/s004450050219

Pierson, T.C. (2005) Hyperconcentrated flow – transitional process between water flow and debris flow. In *Debris-flow Hazards and Related Phenomena*, Jakob, M., Hungr, O. (eds). Springer: Cham; 159–202.

Pierson, T.C., Costa, J.E. & Vancouver, W. (1987) A rheologic classification of subaerial sediment-water flows. In *Debris Flows/Avalanches*, Vol. 7, Costa, JE., Wieczorek, GF. (eds). Geological Society of America: Boulder, CO. https://doi.org/10.1130/REG7-p1

Pierson, T.C., Janda, R.J., Thouret, J.-C. & Borrero, C.A. (1990) Perturbation and melting of snow and ice by the 13 November 1985 eruption of Nevado del Ruiz, Colombia, and consequent mobilization, flow and deposition of lahars. *Journal of Volcanology and Geothermal Research*, 41(1–4), 17–66. https://doi.org/10.1016/0377-0273(90)90082-Q

Pierson, T.C. & Scott, K.M. (1985) Downstream dilution of a lahar: Transition from debris flow to hyperconcentrated streamflow. *Water Resources Research*, 21(10), 1511–1524. https://doi.org/10.1029/WR021i010p01511

Pistolesi, M., Cioni, R., Rosi, M. & Aguilera, E. (2014) Lahar hazard assessment in the southern drainage system of Cotopaxi volcano, Ecuador: Results from multiscale lahar simulations. *Geomorphology*, 207, 51–63. https://doi.org/10.1016/j.geomorph.2013.10.026

Pistolesi, M., Cioni, R., Rosi, M., Cashman, K.V., Rossotti, A. & Aguilera, E. (2013) Evidence for lahar-triggering mechanisms in complex stratigraphic sequences: The post-twelfth century eruptive activity of Cotopaxi Volcano, Ecuador. *Bulletin of Volcanology*, 75(3), 698. https://doi.org/10.1007/s00445-013-0698-1

Pistolesi, M., Rosi, M., Cioni, R., Cashman, K.V., Rossotti, A. & Aguilera, E. (2011) Physical volcanology of the post–twelfth-century activity at Cotopaxi volcano, Ecuador: Behavior of an andesitic central volcano. *Bulletin*, 123, 1193–1215.

Pitman, E.B. & Le, L. (2005) A two-fluid model for avalanche and debris flows. *Philosophical Transactions Series A: Mathematical, Physical, and Engineering Sciences*, 363(1832), 1573–1601. https://doi.org/10.1098/rsta.2005.1596

Prochaska, A.B., Santi, P.M., Higgins, J.D. & Cannon, S.H. (2008) A study of methods to estimate debris flow velocity. *Landslides*, 5(4), 431–444. https://doi.org/10.1007/s10346-008-0137-0

Procter, J.N., Cronin, S.J., Fuller, I.C., Sheridan, M., Neall, V.E. & Keys, H. (2010) Lahar hazard assessment using Titan2D for an alluvial fan with rapidly changing geomorphology: Whangaehu River, Mt. Ruapehu. *Geomorphology*, 116(1–2), 162–174. https://doi.org/10.1016/j.geomorph.2009.10.016

Pudasaini, S.P. & Fischer, J.T. (2016) A mechanical erosion model for two-phase mass flows. *arXiv preprint arXiv:1610.01806*.

Revellino, P., Hungr, O., Guadagno, F.M. & Evans, S.G. (2004) Velocity and runout simulation of destructive debris flows and debris avalanches in pyroclastic deposits, Campania region, Italy. *Environmental Geology*, 45(3), 295–311. https://doi.org/10.1007/s00254-003-0885-z

Rickenmann, D. (1999) Empirical relationships for debris flows. *Natural Hazards*, 19(1), 47–77. https://doi.org/10.1023/A:1008064220727

Salm, B. (1993) Flow, flow transition and runout distances of flowing avalanches. *Annals of Glaciology*, 18, 221–226. https://doi.org/10.3189/S0260305500011551

Schneider, D., Bartelt, P., Caplan-Auerbach, J., Christen, M., Huggel, C. & McArdell, B.W. (2010) Insights into rock-ice avalanche dynamics by combined analysis of seismic recordings and a numerical avalanche model. *Journal of Geophysical Research*, 115, F04026. https://doi.org/10.1029/2010JF001734

Schneider, D., Granados, HD., Huggel, C. & Kääb, A. (2008) Assessing lahars from ice-capped volcanoes using ASTER satellite data, the SRTM DTM and two different flow models: Case study on Iztaccíhuatl (Central Mexico). *Natural Hazards and Earth System Sciences*, 8 (3), 559–571. https://doi.org/10.5194/nhess-8-559-2008

Schneider, D., Huggel, C., Cochachin, A., Guillén, S. & García, J. (2014) Mapping hazards from glacier lake outburst floods based on modelling of process cascades at Lake 513, Carhuaz, Peru. *Advances in Geosciences*, 35, 145–155. https://doi.org/10.5194/adgeo-35-145-2014

Schraml, K., Thomschitz, B., McArdell, B.W., Graf, C. & Kaitna, R. (2015) Modeling debris-flow runout patterns on two alpine fans with different dynamic simulation models. *Natural Hazards and Earth System Sciences*, 15(7), 1483–1492. https://doi.org/10.5194/nhess-15-1483-2015

Schürch, P., Densmore, A.L., Rosser, N.J. & McArdell, B.W. (2011) Dynamic controls on erosion and deposition on debris-flow fans. *Geology*, 39 (9), 827–830. https://doi.org/10.1130/G32103.1

Scott, K.M. (1988) *Origins, behavior, and sedimentology of lahars and lahar-runout flows in the Toutle-Cowlitz River system*. Professional Paper 1447-A.

Scott, K.M., Vallance, J.W., Kerle, N., Luis Macías, J., Strauch, W. & Devoli, G. (2005) Catastrophic precipitation-triggered lahar at Casita volcano, Nicaragua: Occurrence, bulking and transformation. *Earth Surface Processes and Landforms*, 30(1), 59–79. https://doi.org/10.1002/esp.1127

Sierra, D., Vasconez, F., Andrade, S.D., Almeida, M. & Mothes, P. (2019) Historical distal lahar deposits on the remote eastern-drainage of Cotopaxi volcano, Ecuador. *Journal of South American Earth Sciences*, 95, 102251. https://doi.org/10.1016/j.jsames.2019.102251

Small, C. & Naumann, T. (2001) The global distribution of human population and recent volcanism. *Global Environmental Change Part B: Environmental Hazards*, 3(3–4), 93–109. https://doi.org/10.1016/S1464-2867(02)00002-5

Smith, G.A. & Fritz, W.J. (1989) Volcanic influences on terrestrial sedimentation. *Geology*, 17(4), 375–376. https://doi.org/10.1130/0091-7613(1989)017<0375:VIOTS>2.3.CO;2

Sodiro, L. (1877) *Relación sobre la erupción del Cotopaxi acaecida el día 26 de Junio de 1877*.

Sosio, R., Crosta, G.B. & Hungr, O. (2008) Complete dynamic modeling calibration for the Thurwieser rock avalanche (Italian Central Alps). *Engineering Geology*, 100(1–2), 11–26. https://doi.org/10.1016/j.enggeo.2008.02.012

Sosio, R., Crosta, G.B. & Hungr, O. (2011) Numerical modeling of debris avalanche propagation from collapse of volcanic edifices. *Landslides*, 9, 315–334.

Thouret, J.-C., Antoine, S., Magill, C. & Ollier, C. (2020) Lahars and debris flows: Characteristics and impacts. *Earth-Science Reviews*, 201, 103003. https://doi.org/10.1016/j.earscirev.2019.103003

Toapaxi, J., Torres, C., Hamad, K., Vera, P. & Méndez, J. (2019) Actualización de la modelación numérica del flujo de escombros producto de una erupción del volcán Cotopaxi–Flanco Norte. *Revista Politécnica*, 44(1), 7–14. https://doi.org/10.33333/rp.vol44n1.01

Vallance, J.W. & Iverson, R.M. (2015) Lahars and their deposits. In *The Encyclopedia of Volcanoes*. Elsevier: Amsterdam.

Vera, P., Ortega, P., Casa, E., Santamaría, J. & Hidalgo, X. (2019) Modelación numérica y mapas de afectación por flujo de lahares primarios en el drenaje sur del volcán Cotopaxi. *Revista Politécnica*, 43(1), 61–72. https://doi.org/10.33333/rp.vol43n1.971

Vezzoli, L., Apuani, T., Corazzato, C. & Uttini, A. (2017) Geological and geotechnical characterization of the debris avalanche and pyroclastic deposits of Cotopaxi Volcano (Ecuador). *Journal of Volcanology and Geothermal Research*, 332, 51–70. https://doi.org/10.1016/j.jvolgeores.2017.01.004

Voellmy, A. (1955) Ueber die Zersstorungskraft von Lawinen. *Schweizerische Bauzeitung*, 73, 212–217.

Vuille, M., Carey, M., Huggel, C., Buytaert, W., Rabatel, A., Jacobsen, D. *et al.* (2018) Rapid decline of snow and ice in the tropical Andes – impacts, uncertainties and challenges ahead. *Earth-Science Reviews* 176, 195–213. https://doi.org/10.1016/j.earscirev.2017.09.019

Williams, R., Stinton, A. & Sheridan, M. (2008) Evaluation of the Titan2D two-phase flow model using an actual event: Case study of the 2005 Vazcún Valley Lahar. *Journal of Volcanology and Geothermal Research*, 177(4), 760–766. https://doi.org/10.1016/j.jvolgeores.2008.01.045

Wolf, T. (1878) *Memoria sobre El Cotopaxi y su ultima erupcion, acaecida el 26 de junio de 1877*.

Worni, R., Huggel, C., Stoffel, M. & Pulgarín, B. (2011) Challenges of modeling current very large lahars at Nevado del Huila Volcano, Colombia. *Bulletin of Volcanology*, 74, 309–324.

SUPPORTING INFORMATION

Additional supporting information may be found online in the Supporting Information section at the end of this article.

How to cite this article: Frimberger T, Andrade SD, Weber S, Krautblatter M. Modelling future lahars controlled by different volcanic eruption scenarios at Cotopaxi (Ecuador) calibrated with the massively destructive 1877 lahar. *Earth Surf. Process. Landforms*. 2021;46:680–700. https://doi.org/10.1002/esp.5056